Selective Photocatalytic Reduction of CO_2 to CH_4 over NU-1000 Metal-Organic Frameworks

Pekka Korhonen[a]†, Madasamy Thangamuthu[a], Evandro Castaldelli[b], Ander Diego-Lopez[a,c], Andreas Weilhard[a], Rob Clowes[d], James N. O'Shea[e], Andrea Laybourn*[b], Anabel E. Lanterna*[a]

[a]School of Chemistry, University of Nottingham, University Park, NG7 2RD, UK.

[b]Faculty of Engineering, University of Nottingham, University Park, NG7 2RD, UK.

[c]Instituto Mixto de Tecnología Química, Universitat Politècnica de València-Consejo Superior de Investigaciones Científicas, Avda. de Los Naranjos S/n, E-46022, Valencia, Spain

[d] Department of Chemistry and Materials Innovation Factory, University of Liverpool, L69 3BX, UK.

[e] School of Physics, University of Nottingham, University Park, NG7 2RD, UK.

KEYWORDS: CO_2 reduction, photocatalysis, NU-1000, metal-organic frameworks, microwave synthesis

ABSTRACT: CO_2 adsorption and its subsequent utilization represent a promising avenue for mitigating climate change. The conversion of CO_2 into valuable and useful products like carbon monoxide, methane, and methanol offers significant economic benefits. However, due to the low reactivity of CO_2, the incorporation of CO_2 adsorbents alongside catalytic materials has been pivotal in increasing the concentration of CO_2 molecules around the catalytic sites. This strategy frequently relies on the precise deposition of the catalyst onto the adsorbent material. In this work, we explore NU-1000, a zirconium-based metal-organic framework originally designed as a CO_2 adsorbent, to act as a selective photocatalyst for gas-phase CO_2 reduction to CH_4. NU-1000 contains UVA light-absorbing chromophore linkers, endowing it with the dual functionality of CO_2 adsorbent and photocatalyst, which is crucial for efficient CO_2 reutilization. Our research showcases an easily reproducible, and greener synthesis method for NU-1000 using microwaves. We study the activity of NU-1000, including a functionalised variant, in the gas-phase photoreduction of CO_2 to CH_4 at room temperature and atmospheric pressure with electrons and protons derived from water. Remarkably, both the native and functionalised MOFs exhibit a rate of 170 and 800 $\mu mol \cdot g^{-1} \cdot h^{-1}$, respectively, alongside an exceptional selectivity of over 99%. These findings represent some of the highest reported values for gas phase CO_2 photoreduction under atmospheric conditions. Our results provide a foundation for exploring materials that can serve as both catalysts and sorbents in the photocatalytic transformation of CO_2 to value-added products.

Introduction

The Earth's atmospheric CO_2 levels are fast approaching close to critical thresholds, posing severe threats to life on the planet. Combatting climate change involves harnessing CO_2 as a resource in various sectors like chemicals, energy, and materials.[1] Traditional thermal catalytic methods have demonstrated success in converting CO_2 into valuable products like methane (CH_4), methanol (CH_3OH), carbon monoxide (CO) and higher hydrocarbons using transition metal catalysts.[2] However, thermal catalysis comes with significant limitations, including high energy demands due to the need for elevated temperatures (200-500°C), which often result in catalyst deactivation. In recent decades, there has been increasing interest in photocatalytic processes, mimicking natural photosynthesis, to reduce the environmental impact and cost of CO_2 conversion.[1a, 1b] Photocatalytic processes require only solar irradiation and water (acting as a sacrificial electron and H^+ donor), hold promise for converting CO_2 into solar fuels. The main gas phase products include CH_4 and CO, while liquid phase products commonly consist of CH_3OH, formic acid, and formaldehyde.[3] Unfortunately, most photocatalytic process suffers from low selectivity, especially in generating gas phase products, frequently unable to suppress the hydrogen evolution reaction in the presence of water. This limitation obstructs their scalability into large-scale technologies.[4] The photocatalytic reduction of CO_2 typically begins with CO_2 adsorption on the catalyst surface, followed by reduction to active $CO_2^{\bullet-}$ species, initiating various chemical reactions involving multiple electron transfer steps. These reactions commonly result in a range of products, lowering the reaction selectivity.[5] Controlling hydrogen evolution, particularly in liquid-phase reactions with an excess of water compared to CO_2 poses a significant challenge.[6] Increased CO_2 pressure can enhance product formation by boosting CO_2 solubility, but this approach limits the practicality of the process.[7] Gas-phase CO_2 reduction minimises hydrogen formation, but ensuring CO_2 adsorption near the active sites becomes critical to increase the reaction efficiency. Innovative approaches involve mixing CO_2 adsorbents (such as porous materials) with photocatalysts to increase CO_2 and water uptake, thereby improving catalytic performance.[8]

Metal organic frameworks (MOFs) are excellent candidates for CO_2 capture due to their extremely high surface area and adsorption capacity making them also attractive candidates for CO_2 conversion applications.[9] NU-1000 (**Fig. S1**, $Zr_6(\mu_3$-

$OH)_4(\mu_3\text{-}O)_4(H_2O)_4(OH)_4(TBAPy)_2$) presents excellent chemical and thermal stability, boasting a high BET surface area (2320 m^2g^{-1}) and has recently exhibited high selectivity in capturing CO_2 even at low pressure (1 bar).[10] Additionally, the pyrene centre in the TBAPy ligand is a well-known chromophore[11] rendering NU-1000 with a high light absorption coefficient, particularly in the near UV and visible light range, manifesting as a yellow powder. Earlier reports on Zr-based MOFs suggest that the chromophoric linker's excited electrons can migrate via a ligand to metal charge transfer (LMCT) process to the Zr-oxo node, eventually reducing Zr^{IV} to Zr^{III} – a step conducive to activating CO_2 reduction reaction.[12] Furthermore, NU-1000 contains 25-31 Å mesopores (size is dependent on node accessibility and thus activation protocol)[13] which is beneficial for diffusion of reactants in the structure, offering enough space for performing reactions inside the pores.[14] Despite all these advantages, the utilisation of NU-1000 as a photocatalysts remains relatively unexplored. Recent reports have demonstrated its effectiveness in photocatalytic perfluoroalkylation of olefins[15] and oxidation of mustard gas simulant.[16] Various composite materials incorporating NU-1000 or using it as a photocatalyst support have been used for photocatalytic H_2 generation[17] and CO_2 reduction to CO.[18] For instance, Farha et al have used NU-1000 to support Fe-porphyrin photocatalysts for CO_2 reduction,[19] resulting in the formation of 1867 $\mu mol \cdot g^{-1} \cdot h^{-1}$ of CO and 1600 $\mu mol \cdot g^{-1} \cdot h^{-1}$ of H_2 as a by-product. However, limitations such as low selectivity and poor reusability, primarily due to the porphyrin centre leaching, were observed in liquid phase processes.[20] Shifting the reaction to the gas phase could potentially improve CO_2 diffusion within the MOF and reduce water content, thereby improving selectivity. Photocatalytic CO_2 reduction has been performed on different MOF-based catalysts,[21] however, to the best of our knowledge, conversion of CO_2 to CH_4 with high selectivity has not been reported using NU-1000. Here we show that NU-1000 provides a remarkable selectivity towards CH_4 formation (>99%) when subjected to UVA irradiation under standard atmospheric conditions, i.e., room temperature and 1 atm in the presence of water vapour. The introduction of trifluoroacetic acid (TFA) groups to the nodes of NU-1000 leads to a significant increase in CH_4 formation. These findings suggest that the gas adsorption properties of the catalyst are responsible for the unusual selectivity towards methane.

Results and Discussion

Microwave-assisted (MWA) synthesis has emerged as a promising method to reduce the energy consumption of the process in the production of MOFs.[22] Previously, Zr-based MOFs, such as UiO-66, UiO-67 and PCN-222, have been successfully synthesised within an hour using MWA methods, as opposed to the conventional synthesis methods that took up to 18 hours.[23] In our work, we show the applicability of the MWA heating in NU-1000 synthesis, remarkably reducing the synthesis duration from 18 h[24] to 1 h (**Table S2**). The solid obtained via the MWA method exhibited identical crystalline structure and particle morphology to NU-1000 synthesised via conventional heating (**Fig. S2**).[24-25] To optimise the synthesis conditions, we investigated various parameters, such as different concentrations of TFA and benzoic acid (BA) modulators, aiming to decrease the particle size and increase the yield (Table S3). Our findings revealed that employing a BA to metal (BA:M) ratio of 40:1 and a TFA to metal (TFA:M) ratio of 10.5:1 resulted in the formation of rod-shaped particles (**Fig. 1A**) while maintaining the crystal structure of NU-1000 (**Fig. S3**). The reproducibility of Zr-based MOFs has been reported to be a challenge.[24, 26] To test reproducibility, we performed scaling-out experiments simultaneously with multiple batch samples. The results demonstrated the method's reproducibility (**Fig. S2**), enabling the synthesis of up to 1 g of MOF in a single operation with yields >80 % (**Table S3**). Furthermore, these experiments consistently yielded particles with a median length of 1.64 µm with a range between 0.46 and 3.03 µm, and with a median width of 0.49 µm with a range between 0.13 and 1.03 µm (aspect radio median of 3.24 µm with a range between 2.19 and 4.31 µm) as shown in **Fig. S3**.

Coordinatively unsaturated Zr-nodes are known to influence the water stability of NU-1000. Various strategies have been recently introduced to enhance water stability of Zr-MOFs against the capillary forces caused by water desorption.[27] For instance, TFA is known to prevent the reaction of water with uncoordinated nodes, thereby avoiding MOF degradation during solvent evaporation. This modification can not only help preserve the NU-1000 structure but also increase its lifetime when used as photocatalyst in the presence of water vapours. In our research, we further functionalised NU-1000 with TFA to enhance its water stability under photocatalytic condition.[27a] After functionalisation, the particle size and shape (**Fig. 1B**) as well as the crystal structure of NU-1000 remained unchanged, as evident from the PXRD patterns (**Fig. S2**), wherein both NU-1000 and NU-1000-TFA displayed the (100) plane at 2.7 2θ, indicating the presence of mesopores.

The TGA analysis of NU-1000 (**Fig. S4A**) shows two separate weight losses (events) taking place at 25-100 °C and 150-200 °C, attributed to the evaporation of solvent molecules confined within both the micro- and mesopores.[28] These events exhibit reduced significance in NU-1000-TFA (**Fig. S4B**) likely due to blocked node positions, limiting the adsorption of water or solvent molecules inside the pores. In addition, a distinctive weight loss (14.30 wt%) between 300 and 400 is likely due to TFA desorption, corresponding to an average of 3.41 TFA molecules per Zr node. Complementary temperature programmed desorption (TPD) experiments (**Fig. S5**) show desorption of CO_2 (CO) and H_2O from NU-1000-TFA above 300 °C (< 1%, **Table 2**). The TFA content was further analysed via ^{19}F NMR spectroscopy (**Fig. S6**), suggesting an average of 4 TFA molecules per node, which is the theoretical maximum and slightly higher than the obtained ratio (3.8) in an earlier report.[27a] The complete decomposition of NU-1000 and NU-1000-TFA takes place between 430 and 510 °C as previously reported,[29] indicating a linker to node ratio of 1.88:1 and 1.98:1 for NU-1000 and NU-1000-TFA, respectively, nearly aligning with the theoretical value of 2:1.[28] Finally, the CO_2 adsorption capacity of NU-1000 was evaluated gravimetrically[30] via thermogravimetric CO_2 adsorption (**Fig. 1C**). The results show that NU-1000 can uptake 1.4 $mmol \cdot g^{-1}$ of CO_2 when exposed to a pure CO_2 atmosphere at 25 °C and 1 bar (6.3 wt % uptake), in agreement with previous CO_2 isotherms conducted at 1 bar.[10, 31] The incorporation of TFA slightly reduces the CO_2 adsorption, with an uptake of 1.1 $mmol \cdot g^{-1}$ of CO_2 at 25 °C and 1 bar (5.1 wt % uptake).

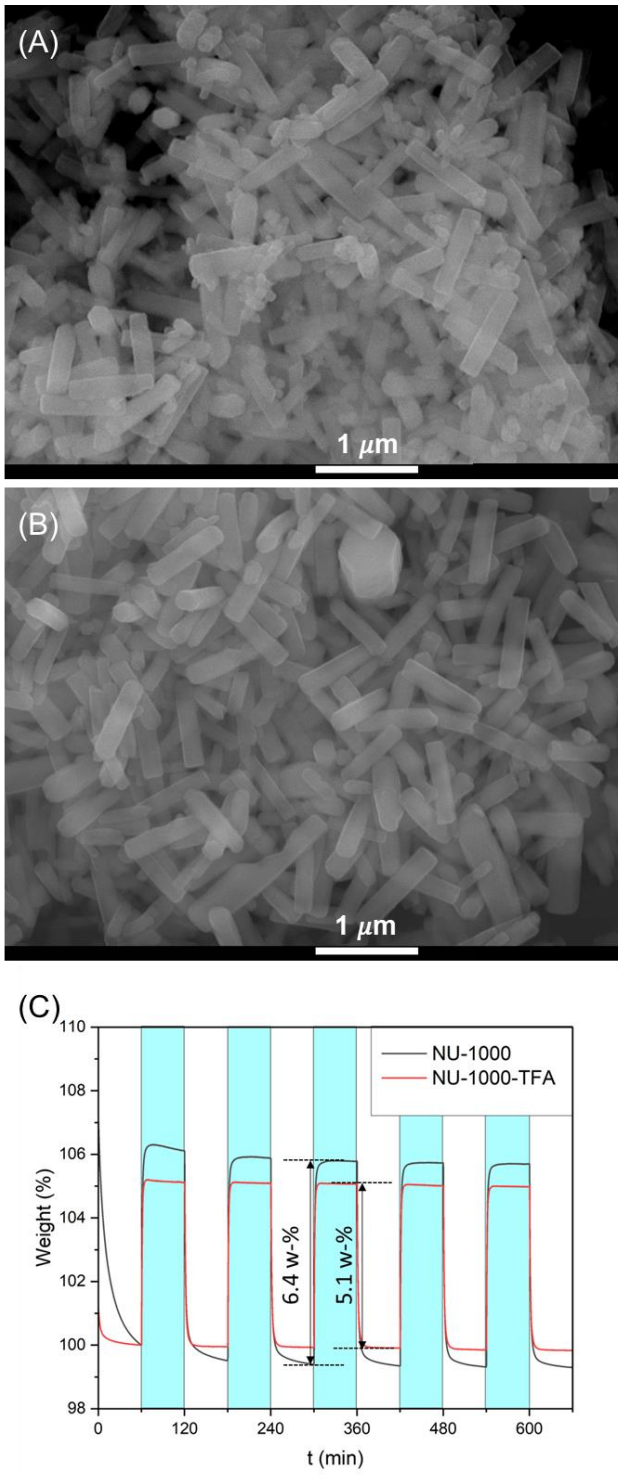

Figure 1. Characterization of NU-1000 and NU-1000-TFA: Representative scanning electron microscopy (SEM) images of (A) NU-1000 and (B) NU-1000-TFA. (C) Gravimetric CO_2 adsorption capacity at 25 °C and 1 bar over 5 adsorption-desorption cycles (adsorption under CO_2, blue shading; and desorption under N_2, white) for NU-1000 (black line) and NU-1000-TFA (red line).

Both NU-1000 and NU-1000-TFA were used for the photocatalytic reduction of CO_2 with water as a source of protons and electrons. Although the use of water is frequently responsible for low CO_2 conversion due to competition with hydrogen evolution, strategic adjustments in water and CO_2 concentrations can circumvent this limitation.[32] Therefore, in our system, photocatalytic CO_2 reduction was carried out in the presence of wet CO_2 (relative humidity ~30%) at atmospheric pressure conditions (**Fig. S7**).[33] Both MOFs present light absorption below 500 nm (**Fig. S8**), enabling the assessment of photocatalytic reduction of CO_2 using UVA (365 nm) and visible light (455 nm) excitation. As shown in Table 1, under UVA light irradiation, both NU-1000 and NU-1000-TFA could exclusively reduce CO_2 to CH_4 as the sole product, with no detection of other carbonaceous products or H_2 (**Fig. S9**). NU-1000-TFA showed a substantially higher average CH_4 production rate of 800 ± 350 $\mu mol \cdot g^{-1} \cdot h^{-1}$ compared to NU-1000 (170 ± 70 $\mu mol \cdot g^{-1} \cdot h^{-1}$) in four repeated experiments. Notably, only the highest recorded CH_4 yield on NU-1000 (290 ± 40 $\mu mol \cdot g^{-1} \cdot h^{-1}$) fell within the same error margin as the lowest yield on NU-1000-TFA (320 ± 30 $\mu mol \cdot g^{-1} \cdot h^{-1}$), suggesting a consistently better performance of NU-1000-TFA. It is important to note here that while functionalisation at the uncoordinated Zr-nodes increases water stability, formate functionalised NU-1000 decreases the catalytic activity for hydrolytic degradation of warfare agents.[13] Thus, our results showing increased CH_4 production when using NU-1000-TFA show a remarkable balance between water uptake, water stability, and Lewis acidity as these influence catalytic activity and sorption properties. When only visible light irradiation (455 nm) is used, 9 and 10 $\mu mol \cdot g^{-1} \cdot h^{-1}$ of CH_4 were generated on NU-1000 and NU-1000-TFA (entries 6 and 13) respectively. No products were observed in the absence of light or catalyst (entries 14-15), suggesting that they are essential for the reaction. Indeed, as shown in **Fig. S10**, as soon as illumination stops, no further CH_4 was formed. These observations conclusively validate CH_4 as the true product of photocatalytic CO_2 reduction on NU-1000 and NU-1000-TFA. The requirement of light irradiation for CH_4 formation proves that this is a photoinduced catalytic process.

Control experiments were conducted by flowing only argon through the reactor, in the absence of water and CO_2 (entries 7 and 16), revealing the presence of average residual CH_4 and CO_2 (**Fig. S10**). These residual carbonaceous compounds arise from material manufacturing and preparation and are commonly adhered to the surface of catalysts.[33-34] The average rate of residual CH_4 released from NU-1000 and NU-1000-TFA under these conditions was 140 ± 60 and 240 ± 130 $\mu mol \cdot g^{-1} \cdot h^{-1}$, respectively. To accurately assess the actual CH_4 formation rate, the values obtained under control conditions were subtracted from the total CH_4 formation rate obtained under reaction conditions (**See Section 1.8, SI**). To further confirm CH_4 is produced from CO_2 reduction we conducted experiments with isotopically labelled $^{13}CO_2$ (**Fig. S11**). The experiments show formation of $^{13}CH_4$, this supports the hypothesis that CH_4 production originates from CO_2 and not from catalyst decomposition.

Table S4 compares the activity of our systems with the highest yields of CH_4 reported under similar (but not identical) reaction conditions. To gauge our photocatalytic systems against commercial TiO_2 (P25), which is reported to yield 50 $\mu mol \cdot g^{-1} \cdot h^{-1}$ of CH_4 and 48 $\mu mol \cdot g^{-1} \cdot h^{-1}$ of H_2, under similar reaction conditions[35], we utilised it as a benchmark for NU-1000 photocatalysts. Notably, residual CH_4 and CO were detected upon irradiating TiO_2 under Ar (**Fig. S9**), however, their production stops after 30 minutes of irradiation. No further production of gases was observed under our reaction conditions (**Fig. S10A**). This phenomenon is suggested to arise due to the low CO_2 adsorption capacity of TiO_2[36].

The stability of NU-1000 and NU-1000-TFA under photocatalytic reaction conditions was evaluated by performing catalyst recycling experiments. Results from Table 1, entries 2-4, indicated a significant decrease in CH_4 yield after three catalytic cycles when NU-1000 was used as catalyst. Additionally, the NU-1000 displayed a noticeable colour change from bright to darker yellow (**Fig. S10E-F**), and PXRD analyses revealed slight broadening of the diffraction peaks while maintaining the crystalline structure after four reactions cycles (**Fig. 2**). This colour change could potentially stem from prolonged exposure to the UV light (16 h), or a combination of UV light and water vapour. To determine if there was permanent damage to the MOFs, we subjected both materials to drying conditions (80 °C overnight). Remarkably, NU-1000 recovered its photocatalytic activity (Table 1, c.f. entries 4 and 5), suggesting that the presence of water might be responsible for the apparent loss of activity. Earlier reports suggest NU-1000 may collapse if dried from a water suspension due to the strong interactions between water molecules and the nodes.[37],[20] Furthermore, Zr-MOFs with coordinatively unsaturated sites on the nodes have shown a decline in crystallinity and water uptake capacity even in a second adsorption cycle, indicating that water promotes structural collapse.[27a],[38] Conversely, the activity recovery is less pronounced when using NU-1000-TFA (Table 1, c.f. entries 11 and 12) however, its activity seems to plateau to slightly above NU-1000 activity after three catalytic cycles (Table 1, c.f. entries 5 and 12).

FT-IR spectroscopy (**Fig. S12**) shows a distinct OH-stretching peak (~3200 cm^{-1}) originating from adsorbed water[39] on NU-1000. This peak appears more pronounced in fresh NU-1000 compared with NU-1000 after photocatalysis which we ascribe to a higher relative humidity in laboratory environment compared with the photocatalytic reaction conditions. The OH-stretching peak for NU-1000-TFA (fresh and post-reaction) exhibits significantly lower intensity, as expected, as TFA inhibits water adsorption on the nodes. The peak at 1204 cm^{-1} corresponding to CF_3[40] in the FT-IR spectra of NU-1000-TFA is slightly reduced after exposing the NU-1000-TFA to photocatalytic reaction conditions (**Fig. S12C**). Marked changes (broadening and reduction in intensity) in peaks in the range of 1411 cm^{-1} and 1666 cm^{-1} corresponding to carbonyl stretching are also observed in the spectra of NU-1000 and NU-1000-TFA after photocatalysis. These differences are also reported for NU-1000[41] and may result from changes in TFA groups, altering the Zr-node environment to resemble the unsaturated nodes in NU-1000. Comparable activity of both catalysts on the fourth reaction cycle (**Fig. S10B**) after initially better activity of NU-1000-TFA supports this hypothesis.

Table 1. Optimisation of the photocatalytic reduction of CO_2.[a]

Entry	Catalyst	Run	Condition-changes	CH_4 yield ($\mu mol \cdot g^{-1} \cdot h^{-1}$)
1	NU-1000	Average	-	170 ± 70
2	NU-1000[b]	1	-	170 ± 10
3	NU-1000[b]	2	-	226 ± 7
4	NU-1000[b]	3	-	62 ± 5
5	NU-1000[c]	4	Overnight drying	161 ± 5
6	NU-1000[d]	1	450 nm	9 ± 2
7	NU-1000[f]	Average	No CO_2	140 ± 60
8	NU-1000-TFA	Average	-	800 ± 350
9	NU-1000-TFA[b]	1	-	320 ± 30
10	NU-1000-TFA[b]	2	-	400 ± 25
11	NU-1000-TFA[b]	3	-	182 ± 5
12	NU-1000-TFA[c]	4	Overnight drying	200 ± 2
13	NU-1000-TFA[d]	1	450 nm	10 ± 1
14	None	1	-	0
15	NU-1000-TFA[e]	1	dark	0
16	NU-1000-TFA[f]	Average	No CO_2	200 ± 130
17	NU-1000-TFA[g]	1	No CO_2	170 ± 10
18	TiO_2 (P25)	1	-	Traces

[a]Reaction conditions: catalyst (area: ~2 cm^2, thickness: 22 μm, mass: 300 μg), Ar (1 sccm), wet CO_2 (1 sccm) (RH ~30%), 365 nm LED irradiation (1.8 Wcm^{-2}, ~1 cm^2 spot). [b]Sample recycled as shown in **Fig. S10**. [c]Reactivated via overnight drying treatment. [d]Visible light irradiation (450 nm LED working at 1.46 W cm^{-1}). [e]Dark. [f]No CO_2, Ar (2 sccm). [g]No CO_2, wet Ar (1 sccm). Average corresponds to mean values found between four different runs.

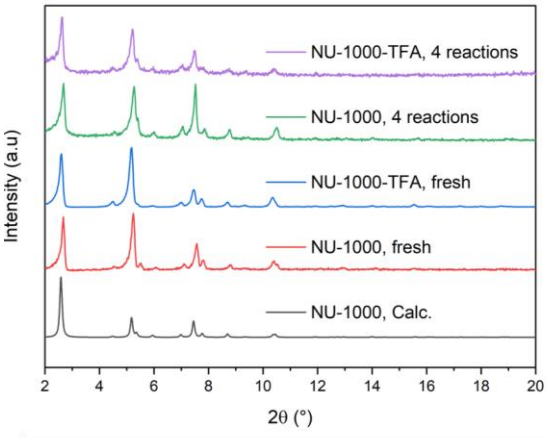

Figure 2. PXRD patterns of the catalyst on FTO slides before (fresh) and after 4 CO_2 reduction cycles compared with the calculated PXRD pattern for NU-1000 from CCDC-955328.[42] con

SEM images of NU-1000 and NU-1000-TFA on the FTO slides before and after CO_2 reduction (**Fig. S13**) show similar rod-shaped morphology, as reported before[27a]. However, a contraction of particles for both MOFs is clearly visible after the photocatalytic reaction. Statistical analysis of particle dimensions, presented as box and whisker plots (**Fig. S14**) demonstrates that NU-1000 experienced a contraction in length between cycle 1 and 4 (median is reduced from 0.85 to 0.54 μm) and a continual contraction of width from fresh to cycle 1 to cycle 4 (median value of 0.21 to 0.14 to 0.09 μm). NU-1000-TFA exhibited a contraction in length between fresh and cycle 1 (median value of 0.86 c.f. 0.56 μm) and a contraction in width from fresh to cycle 1 to 4 (median of 0.21 to 0.13 to 0.12 μm). Additionally, the PXRD pattern of NU-1000 shows an increase in the intensity of the peak at *ca.* 7.5 degrees 2θ after photocatalysis. Previous studies have investigated MOF contraction and expansion and observed structural changes in both NU-1000 and functionalised NU-1000, including structural transitions in the Zr-nodes

due to dehydration/dihydroxylation,[43] temperature-dependent expansion and contraction,[44] and pore channel contraction due to water evaporation.[41] These changes in structure coincide with a reduced photocatalytic activity for both MOFs, potentially due to a decline in porosity and likely caused by a combination of water and UVA irradiation.

Both MOF systems show a remarkable selectivity towards CH_4. To better understand this, we conducted TPD experiments in both NU-1000 and NU-1000-TFA (**Fig. S5**) prior to catalysis. The analysis revealed the presence of H_2O, CO_2, CO and CH_4 in both material, accounting for the residual amounts of CH_4 observed under irradiation but in the absence of external CO_2 (**Table 2**). These findings align with the slightly higher CO_2 adsorption detected on NU-1000 in the TGA experiments (**Fig. 1C**). Table 3 shows the desorption temperatures for each compound. CO_2 and CO exhibit similar desorption profiles, implying that CO might originate from CO_2 decomposition during the TPD analysis. CO_2 and CO desorption from NU-1000-TFA occurred at higher temperatures (> 250 °C) compared to NU-1000 (< 180 °C). Analysis of the signal ratio between mass 44 (CO_2) and mass 28 (CO) indicates that CO is formed by decomposition of CO_2 under TPD conditions. This conclusion is supported by the absence of CO observed during blank conditions, where CO_2 and CH_4 were detected by GC-FID (**Fig. S9**). There are two peaks corresponding to water desorption, which can be ascribed to free water in the pore and water bound at the Zr-node. A clear reduction in water signal between NU-1000 and NU-1000-TFA indicates that substantially less water release from NU-1000-TFA, further supporting the hypothesis that TFA functionalisation hinders water adsorption at the Zr-nodes. Furthermore, the temperatures at which water is desorbed in NU-1000-TFA (275 °C and >350 °C) are much higher than in NU-1000 (164 °C and 234 °C). This might affect the CO_2 to H_2O ratio during the reaction (due to competitive sorption), which could explain the different reactivity found in the initial stages of the NU-1000-TFA catalyst. Notably, loosely bound water molecules are desorbed at low temperatures (< 100 °C) for both NU-1000 and NU-1000-TFA, which could explain why the activity of both catalysts is restored after drying them at 80 °C. Finally, CH_4 desorption profiles show two separate events, possibly attributed to desorption from different pores (micro- vs. meso-pores). Interestingly, NU-1000-TFA releases methane at temperatures <73 °C, while NU-1000 does so at temperatures >110 °C. This suggests slightly stronger binding of CH_4 on NU-1000 than NU-1000-TFA,[45] ultimately contributing to the overall selectivity towards this product under the photocatalytic conditions. As both, CO_2 and CO seem to be retained in the MOFs better (higher temperatures needed to desorb them), their dwell time close to the catalytic sites might be longer, allowing for further reduction process to take place. Weaker binding of CH_4 means easier desorption of the product, which can contribute to higher detected CH_4 yield as formed CH_4 is released more easily. Heats of adsorption of different gases on NU-1000 have been investigated earlier, suggesting stronger bonding of CO than CH_4 in low concentrations at -196 °C[46], showing similar trend as our results.

Table 2. TPD analysis of NU-1000 and NU-1000-TFA showing the amount of each compound detected.

Compound	NU-1000 ($mL\ g_{cat}^{-1}$)	NU-TFA-1000 ($mL\ g_{cat}^{-1}$)
CO_2	1.45	0.99
CO	0.47	0.31
CH_4	0.05	0.07

Table 3. TPD analysis of NU-1000 and NU-1000-TFA showing the desorption temperatures for each compound.

Compound	NU-1000 (°C)*	NU-TFA-1000 (°C)*
CO_2	180 185 212	300 321 >350
CO	180 185 212	300 321 >350
H_2O	164 234	275 >350
CH_4	122 274	73 164

*±2 °C.

CONCLUSION

In conclusion, we have developed a simple and reproducible MWA method for NU-1000 synthesis that substantially reduces both time (from 18 h to 1 h) and energy demands, making the synthesis greener and more sustainable compared to conventionally heated methods. We have demonstrated the NU-1000's dual functionality, serving as an effective CO_2 adsorbent and photocatalyst for gas phase CO_2 reduction. Moreover, we have shown how the catalyst's activity can be increased by TFA functionalisation. Our exploration of the photocatalytic properties of both NU-1000 and its TFA-functionalised analogue, under UVA light and atmospheric conditions, resulted in impressive CH_4 production rates of 170 and 800 $\mu mol \cdot g^{-1} \cdot h^{-1}$, respectively, with a remarkable selectivity >99%. Temperature programmed gas desorption studies suggest that this selectivity is due to different affinities for CO_2 versus CH_4, with the latter starting to desorb at temperatures as low as 50 °C. These results set significant precedent for investigating materials capable of simultaneously acting as catalysts and sorbents for photocatalytic transformation of CO_2 to value added products.

ASSOCIATED CONTENT

Supporting Information

The Supporting Information PDF is available free of charge on the ACS Publications website.

AUTHOR INFORMATION

Corresponding Authors

*AEL: anabel.lanterna@nottingham.ac.uk
*AL: andrea.laybourn@nottingham.ac.uk

Author Contributions

The manuscript was written through contributions of all authors. All authors have given approval to the final version of the manuscript.

Funding Sources

This work was supported by the Engineering and Physical Sciences Research Council (EPSRC) Programme grant MASI (EP/V000055/1) and the EPSRC and Science Foundation Ireland (SFI) Centre for Doctoral Training in Sustainable Chemistry: Atoms-2-Products an Integrated Approach to Sustainable Chemistry (EP/S022236/1). SEM analyses were supported by the EPSRC and the University of Nottingham.

Notes

†In memory of Pekka Korhonen (DOD: 23rd October 2023), a dedicated scientist and exceptional friend.

ACKNOWLEDGMENT

The authors give thanks to and acknowledge funding from the Engineering and Physical Sciences Research Council (EPSRC) and Science Foundation Ireland (SFI) Centre for Doctoral Training in Sustainable Chemistry: Atoms-2-Products an Integrated Approach to Sustainable Chemistry (Grant number: EP/S022236/1) and the EPSRC Programme grant MASI (EP/V000055/1). AL and EC gratefully acknowledge funding from EPSRC (EP/V055410/1). ADL is grateful to the Universitat Politècnica de València for the Predoctoral FPI fellowship (FPI-UPV/Subprograma 1). The authors thank the Nanoscale and Microscale Research Centre (nmRC) for providing access to instrumentation and Dr. Michael W. Fay for technical assistance. Additional thanks go to Mr Mark Guyler for all the technical support and Dr. Kevin Butler for helping in collection of NMR data. We thank the Nottingham Applied materials and Interfaces (NAMI) group for access to mass spectrometry and Dr. Jack Jordan and Mr. Benjamin Denison for their assistance.

REFERENCES

[1] [a]E. Gong, S. Ali, C. B. Hiragond, H. S. Kim, N. S. Powar, D. Kim, H. Kim, S.-I. In, *Energy Env. Sci.* **2022**, *15*, 880-937; [b]J. Q. Lv, J. F. Xie, A. G. A. Mohamed, X. Zhang, Y. Y. Feng, L. Jiao, E. B. Zhou, D. Q. Yuan, Y. B. Wang, *Nat. Rev. Chem.* **2023**, *7*, 91-105; [c]H. B. Gray, *Nat. Chem.* **2009**, *1*, 7-7.

[2] [a]W. K. Fan, M. Tahir, *J. Environ. Chem. Eng.* **2021**, *9*, 105460; [b]W. J. Lee, C. Li, H. Prajitno, J. Yoo, J. Patel, Y. Yang, S. Lim, *Catal. Today* **2021**, *368*, 2-19; [c]R.-P. Ye, J. Ding, W. Gong, M. D. Argyle, Q. Zhong, Y. Wang, C. K. Russell, Z. Xu, A. G. Russell, Q. Li, M. Fan, Y.-G. Yao, *Nat. Comm.* **2019**, *10*, 5698; [d]I. U. Din, M. S. Shaharun, M. A. Alotaibi, A. I. Alharthi, A. Naeem, *J. CO2 Util.* **2019**, *34*, 20-33.

[3] N. Shehzad, M. Tahir, K. Johari, T. Murugesan, M. Hussain, *J. CO2 Util.* **2018**, *26*, 98-122.

[4] J. Fu, K. Jiang, X. Qiu, J. Yu, M. Liu, *Mater. Today* **2020**, *32*, 222-243.

[5] H.-N. Wang, Y.-H. Zou, H.-X. Sun, Y. Chen, S.-L. Li, Y.-Q. Lan, *Coord. Chem. Rev.* **2021**, *438*, 213906.

[6] A. Olivo, E. Ghedini, M. Signoretto, M. Compagnoni, I. Rossetti, *Energies* **2017**, *10*, 1394.

[7] I. Rossetti, A. Villa, M. Compagnoni, L. Prati, G. Ramis, C. Pirola, C. L. Bianchi, W. Wang, D. Wang, *Cat. Sci. Tech.* **2015**, *5*, 4481-4487.

[8] D. Li, M. Kassymova, X. Cai, S.-Q. Zang, H.-L. Jiang, *Coord. Chem. Rev.* **2020**, *412*.

[9] M. Ding, R. W. Flaig, H. L. Jiang, O. M. Yaghi, *Chem. Soc. Rev.* **2019**, *48*, 2783-2828.

[10] J. H. Kang, T.-U. Yoon, S.-Y. Kim, M.-B. Kim, H.-J. Kim, H.-C. Yang, Y.-S. Bae, *Microporous Mesoporous Mater.* **2019**, *281*, 84-91.

[11] A. J. Howarth, M. B. Majewski, M. O. Wolf, *Coord. Chem. Rev.* **2015**, *282-283*, 139-149.

[12] [a]D. Sun, Y. Fu, W. Liu, L. Ye, D. Wang, L. Yang, X. Fu, Z. Li, *Chemistry* **2013**, *19*, 14279-14285; [b]G. Zhai, Y. Liu, L. Lei, J. Wang, Z. Wang, Z. Zheng, P. Wang, H. Cheng, Y. Dai, B. Huang, *ACS Catal.* **2021**, *11*, 1988-1994; [c]L. Xia, W. Zhou, Y. Xu, Z. Xia, X. Wang, Q. Yang, G. Xie, S. Chen, S. Gao, *Chem. Eng. J.* **2023**, *451*; [d]H. Q. Xu, J. Hu, D. Wang, Z. Li, Q. Zhang, Y. Luo, S. H. Yu, H. L. Jiang, *J. Am. Chem. Soc.* **2015**, *137*, 13440-13443; [e]Y. Benseghir, A. Solé-Daura, D. R. Cairnie, A. L. Robinson, M. Duguet, P. Mialane, P. Gairola, M. Gomez-Mingot, M. Fontecave, D. Iovan, B. Bonnett, A. J. Morris, A. Dolbecq, C. Mellot-Draznieks, *J. Mater. Chem. A* **2022**, *10*, 18103-18115; [f]E. S. Gutterød, S. H. Pulumati, G. Kaur, A. Lazzarini, B. G. Solemsli, A. E. Gunnæs, C. Ahoba-Sam, M. E. Kalyva, J. A. Sannes, S. Svelle, E. Skúlason, A. Nova, U. Olsbye, *J. Am. Chem. Soc.* **2020**, *142*, 17105-17118.

[13] Z. Lu, J. Liu, X. Zhang, Y. Liao, R. Wang, K. Zhang, J. Lyu, O. K. Farha, J. T. Hupp, *J. Am. Chem. Soc.* **2020**, *142*, 21110-21121.

[14] T. E. Webber, W. G. Liu, S. P. Desai, C. C. Lu, D. G. Truhlar, R. L. Penn, *ACS App. Mater. Inter.* **2017**, *9*, 39342-39346.

[15] T. Zhang, P. Wang, Z. Gao, Y. An, C. He, C. Duan, *RSC Adv.* **2018**, *8*, 32610-32620.

[16] Y. Liu, C. T. Buru, A. J. Howarth, J. J. Mahle, J. H. Buchanan, J. B. DeCoste, J. T. Hupp, O. K. Farha, *J. Mater. Chem. A* **2016**, *4*, 13809-13813.

[17] [a]P. P. Bag, X.-S. Wang, P. Sahoo, J. Xiong, R. Cao, *Cat. Sci. Tech.* **2017**, *7*, 5113-5119; [b]A. W. Peters, Z. Li, O. K. Farha, J. T. Hupp, *ACS App. Mater. Inter.* **2016**, *8*, 20675-20681; [c]L. Jiao, Y. Dong, X. Xin, L. Qin, H. Lv, *App. Catal., B:* **2021**, *291*, 120091.

[18] P. M. Stanley, A. Y. Su, V. Ramm, P. Fink, C. Kimna, O. Lieleg, M. Elsner, J. A. Lercher, B. Rieger, J. Warnan, R. A. Fischer, *Adv. Mater.* **2023**, *35*, 2207380.

[19] K. Zhang, S. Goswami, H. Noh, Z. Lu, T. Sheridan, J. Duan, W. Dong, J. T. Hupp, *J. Photochem. Photobiol.* **2022**, *10*, 100111.

[20] J. E. Mondloch, M. J. Katz, N. Planas, D. Semrouni, L. Gagliardi, J. T. Hupp, O. K. Farha, *Chem. Commun.* **2014**, *50*, 8944-8946.

[21] [a]Z. B. Fang, T. T. Liu, J. Liu, S. Jin, X. P. Wu, X. Q. Gong, K. Wang, Q. Yin, T. F. Liu, R. Cao, H. C. Zhou, *J. Am. Chem. Soc.* **2020**, *142*, 12515-12523; [b]R. R. Ikreedeegh, M. Tahir, *J. Environ. Chem. Eng.* **2021**, *9*, 105600; [c]H. B. Huang, Z. B. Fang, R. Wang, L. Li, M. Khanpour, T. F. Liu, R. Cao, *Small* **2022**, *18*, e2200407.

[22] [a]I. Thomas-Hillman, A. Laybourn, C. Dodds, S. W. Kingman, *J. Mater. Chem. A* **2018**, *6*, 11564-11581; [b]I. Thomas-Hillman, L. A. Stevens, M. Lange, J. Möllmer, W. Lewis, C. Dodds, S. W. Kingman, A. Laybourn, *Green Chem.* **2019**, *21*, 5039-5045.

[23] [a]Y. Li, Y. Liu, W. Gao, L. Zhang, W. Liu, J. Lu, Z. Wang, Y.-J. Deng, *CrystEngComm* **2014**, *16*, 7037-7042; [b]R. Vakili, S. Xu, N. Al-Janabi, P. Gorgojo, S. M. Holmes, X. Fan, *Microporous Mesoporous Mater.* **2018**, *260*, 45-53; [c]S. Carrasco, A. Sanz-Marco, B. Martín-Matute, *Organomet.* **2019**, *38*, 3429-3435.

[24] T. Islamoglu, K. Otake, P. Li, C. T. Buru, A. W. Peters, I. Akpinar, S. J. Garibay, O. K. Farha, *CrystEngComm* **2018**, *20*, 5913-5918.

[25] [a]T. E. Webber, S. P. Desai, R. L. Combs, S. Bingham, C. C. Lu, R. L. Penn, *Cryst. Growth Des.* **2020**, *20*, 2965-2972; [b]P. K. Verma, L. Huelsenbeck, A. W. Nichols, T. Islamoglu, H. Heinrich, C. W. Machan, G. Giri, *Chem. Mater.* **2020**, *32*, 10556-10565.

[26] H. L. B. Bostrom, S. Emmerling, F. Heck, C. Koschnick, A. J. Jones, M. J. Cliffe, R. Al Natour, M. Bonneau, V. Guillerm, O. Shekhah, M. Eddaoudi, J. Lopez-Cabrelles, S. Furukawa, M. Romero-Angel, C. Marti-Gastaldo, M. Yan, A. J. Morris, I. Romero-Muniz, Y. Xiong, A. E. Platero-Prats, J. Roth, W. L. Queen, K. S. Mertin, D. E. Schier, N. R. Champness, H. H. Yeung, B. V. Lotsch, *Adv. Mater.* **2023**, e2304832.

[27] [a]L. Yang, K. B. Idrees, Z. Chen, J. Knapp, Y. Chen, X. Wang, R. Cao, X. Zhang, H. Xing, T. Islamoglu, O. K. Farha, *ACS App. Nano Mater.* **2021**, *4*, 4346-4350; [b]J. Liu, R. Anderson, K. M. Schmalbach, T. R. Sheridan, Z. Wang, N. M. Schweitzer, A. Stein, N. A. Mara, D. Gomez-Gualdron, J. T. Hupp, *J. Mater. Chem. A* **2022**, *10*, 17307-17316.

[28] I. A. Lázaro, *Eur. J. Inorg. Chem.* **2020**, *2020*, 4284-4294.

[29] A. J. Howarth, A. W. Peters, N. A. Vermeulen, T. C. Wang, J. T. Hupp, O. K. Farha, *Chem. Mater.* **2016**, *29*, 26-39.

[30] M. G. Plaza, C. Pevida, B. Arias, J. Fermoso, A. Arenillas, F. Rubiera, J. J. Pis, *J. Therm. Anal. Calorim.* **2008**, *92*, 601-606.

[31] [a]P. Deria, J. E. Mondloch, E. Tylianakis, P. Ghosh, W. Bury, R. Q. Snurr, J. T. Hupp, O. K. Farha, *J. Am. Chem. Soc.* **2013**, *135*, 16801-16804; [b]X. Xia, G. Hu, W. Li, S. Li, *ACS App. Nano Mater.* **2019**, *2*, 6022-6029.

[32] [a]M. Tahir, N. S. Amin, *App. Catal., B:* **2013**, *142-143*, 512-522; [b]M. Tahir, N. S. Amin, *App. Catal., B:* **2015**, *162*, 98-109.

[33] M. Dilla, R. Schlögl, J. Strunk, *ChemCatChem* **2017**, *9*, 696-704.

[34] [a]S. Ali, M. C. Flores, A. Razzaq, S. Sorcar, C. B. Hiragond, H. R. Kim, Y. H. Park, Y. Hwang, H. S. Kim, H. Kim, E. H. Gong, J. Lee, D. Kim, S.-I. In, *Catalysts* **2019**, *9*, 727; [b]K. Zhang, Q. Gao, C. Xu, D. Zhao, Q. Zhu, Z. Zhu, J. Wang, C. Liu, H. Yu, C. Sun, X. Liu, Y. Xuan, *Carbon Neutrality* **2022**, *1*, 1.

[35] S. Neatu, J. A. Macia-Agullo, P. Concepcion, H. Garcia, *J. Am. Chem. Soc.* **2014**, *136*, 15969-15976.

[36] M. Ota, Y. Hirota, Y. Uchida, N. Nishiyama, *Colloids Interfaces* **2018**, *2*, 25.

[37] P. Deria, Y. G. Chung, R. Q. Snurr, J. T. Hupp, O. K. Farha, *Chem. Sci.* **2015**, *6*, 5172-5176.

[38] Y. Chen, K. B. Idrees, M. R. Mian, F. A. Son, C. Zhang, X. Wang, O. K. Farha, *J. Am. Chem. Soc.* **2023**, *145*, 3055-3063.

[39] T. Hiraoka, S. Shigeto, *Phys. Chem. Chem. Phys.* **2020**, *22*, 17798-17806.

[40] K. Yamauchi, Y. Yao, T. Ochiai, M. Sakai, Y. Kubota, G. Yamauchi, *J. Nanotechnol.* **2011**, *2011*, 1-7.
[41] Z. Lu, J. Duan, H. Tan, L. Du, X. Zhao, R. Wang, S. Kato, S. Yang, J. T. Hupp, *J. Am. Chem. Soc.* **2023**, *145*, 4150-4157.
[42] X. Gong, L. Xu, S. Huang, X. Kou, S. Lin, G. Chen, G. Ouyang, *Anal. Chim. Acta* **2022**, *1218*, 339982.
[43] A. E. Platero-Prats, A. Mavrandonakis, L. C. Gallington, Y. Liu, J. T. Hupp, O. K. Farha, C. J. Cramer, K. W. Chapman, *J. Am. Chem. Soc.* **2016**, *138*, 4178-4185.
[44] Z. Chen, G. D. Stroscio, J. Liu, Z. Lu, J. T. Hupp, L. Gagliardi, K. W. Chapman, *J. Am. Chem. Soc.* **2023**, *145*, 268-276.
[45] D. A. King, *Surf. Sci.* **1975**, *47*, 384-402.
[46] G. O. Vissers, W. Zhang, O. E. Vilches, W.-G. Liu, H. S. Yu, D. G. Truhlar, C. T. Campbell, *J. Phys. Chem. C* **2019**, *123*, 6586-6591.

Selective Photocatalytic Reduction of CO_2 to CH_4 over NU-1000 Metal-Organic Frameworks

Pekka Korhonen[a], Madasamy Thangamuthu[a], Evandro Castaldelli[b], Ander Diego-Lopez[a,c], Andreas Weilhard[a], Rob Clowes[d], James N. O'Shea[e], Andrea Laybourn*[b], Anabel E. Lanterna*[a]

[a]School of Chemistry, University of Nottingham, University Park, NG7 2RD, UK.

[b]Faculty of Engineering, University of Nottingham, University Park, NG7 2RD, UK.

[c]Instituto Mixto de Tecnología Química, Universitat Politècnica de València-Consejo Superior de Investigaciones Científicas, Avda. de Los Naranjos S/n, E-46022, Valencia, Spain

[d] Department of Chemistry and Materials Innovation Factory, University of Liverpool, L69 3BX, UK.

[e] School of Physics, University of Nottingham, University Park, NG7 2RD, UK.

Table of Contents

1 Experimental Procedures

1.1 Materials

Tetrakis(p-benzoic-acid)pyrene (TBAPy, >97%) was purchased from AmBeed and Key Organics. $ZrOCl_2 \cdot 8H_2O$ (99.9%) and ZrO_2 were obtained from Alfa Aesar. Benzoic acid (99%) and 2-fluorobenzoic acid (2-FBA, 99%) were bought from Acros Chemicals. Synthesis grade trifluoroacetic acid (TFA) was bought from Merck and Honeywell. N,N-Dimethylformamide (DMF), hydrochloric acid (HCl, 37%), absolute ethanol (99.8%), nitric acid (HNO_3, 68%), sulphuric acid (H_2SO_4, 98%) were bought from Fischer Chemicals. 2-propanol (99.9%), acetone (99.5%), D_2SO_4, deuterated DMSO and P25 TiO_2 (99.5%, 21 nm mean particle size) were bought from Sigma Aldrich. Deionised water was obtained from a milli-Q Advantage A10 deioniser. Fluorine doped tin oxide (FTO) coated glass slides were purchased from Ossila Ltd.

1.2 Instruments

Microwave-assisted (MWA) synthesis of NU-1000 ($Zr_6(\mu_3\text{-}OH)_4(\mu_3\text{-}O)_4(H_2O)_4(OH)_4(TBAPy)_2$) MOF was carried out in a Flexiwave MA186 microwave reactor (maximum forward power 900 W) operated in sealed, Teflon high-pressure tubes with a PTFE stirring bar for mixing.

Fourier transform infrared (FT-IR) spectra were recorded using a Bruker Alpha FTIR instrument equipped with single reflection ATR Platinum module between 400-4000 cm^{-1} with 1 s scanning time repeating 25 times.

^{1}H NMR and ^{19}F NMR spectra were measured using a Bruker AV400 NMR instrument at 400 MHz and 376.44 MHz frequency, respectively, and 16 scans. Samples were prepared by digesting about 1 mg of the MOF in 5 droplets of D_2SO_4 which was diluted in 0.75 mL of deuterated DMSO. For ^{19}F NMR, 100 µL of trifluorotoluene was added as an internal standard to quantify the amount of TFA in the sample.

Solid state UV/Vis spectroscopy was performed in an Agilent Cary 5000 UV/Vis/NIR spectrometer using diffuse reflectance accessory within 200-800 nm scanning at 10 nm s^{-1}. Each sample was analysed in triplicate.

Photoluminescence (PL) spectroscopy was measured in an Edinburgh Instruments FLS980 Photoluminescence spectrometer using quartz cuvettes. Spectra were recorded at 1 nm s^{-1} from an average of 3 measurements using a scan slit and offset slit of 0.5 nm, excitation wavelength at 400 nm, and emission range from 450 nm to 700 nm.

Thermogravimetric Analysis (TGA) was performed in a TA Q500 thermogravimetric analyser using platinum sample pans. The samples were heated from 25 to 1000 °C under air or Ar with a flow rate of 60 sccm and a temperature ramp of 10 °C min^{-1}. All samples were kept isothermally at 25 °C before the ramp to 1000 °C to minimise the recorded material loss by other factors than the temperature.

Isothermal gravimetric CO_2 adsorption was measured using a TA TGA550 Discovery thermogravimetric analyser. The samples were first held under a N_2 flow for 60 min and N_2 was changed to CO_2 for 60 min, followed by N_2 flow for 60 min. The 120 min isothermal cycle was repeated for a total of 5 times. Flow rate for N_2 and CO_2 was 100 sccm.

Temperature programmed desorption (TPD) experiments were performed in a Hiden CatLab microreactor and mass signal of pre-determined molar masses were measured by Hiden QGA mass spectrometer. Approximately 10 mg of sample was first loaded into a reactor tube immobilizing it between two quartz wool layers. The sample was then heated with 10 °C min^{-1} rate up to 350 °C.

Powder X-ray diffraction (PXRD) patterns were recorded using PANalytical Xpert MPD X-ray Diffractometer in Bragg-Brentano geometry with PIXcel area detector and sealed tube Cu X-ray source operating at 40 kV and 40 mA. A Johansson focussing beam monochromator was used selecting pure $K_{\alpha 1}$ radiation passing through 0.04 rad Soller slits. All samples were recorded from 2 to 60 degrees (2θ) with 15 mm beam slit to focus the beam into the sample during 20 min and repeated 3 times. Sample powder was placed

on glass sample holders. MOF samples deposited on glass slides (thin films) were analysed by holding the slides in a regular holder.

Scanning Electron Microscopy (SEM) and Energy Dispersive X-ray analysis (EDX) were used to investigate morphology and particle size for the MOFs using a JEOL 7000F FEG-SEM microscope with 15 kV accelerating voltage, probe current set to 8 nA an LED Filter set to 3 and an imaging distance of 10 mm. All samples were placed on 12.5 mm SEM grids on a double-sided tape and coated with 10 nm carbon layer to avoid electrical charging using a Quorum W150R ES sputter coater. EDX signals were collected on an Oxford Instruments EDX detector.

CO_2 conversion was followed by an inline Thermo Scientific Trace1300 gas chromatograph (GC), equipped with thermal conductivity (TCD) and flame ionisation (FID) detectors. Illumination was performed using a Luzchem LEDi system coupled to a 365 nm LED head.

Isotope-tracer experiments with $^{13}CO_2$ were followed by online mass spectrometry using the HALO 201 mass spectrometer from Hiden Analytical.

1.3 NU-1000 synthesis

MWA synthesis of NU-1000 was performed as follows: $ZrOCl_2$ (200 mg) and benzoic acid (3.0 g) were dissolved in DMF (40 mL) in a 100 mL microwave tube. The mixture was heated in a microwave reactor (multimode Flexiwave MA186 microwave reactor, maximum forward power 900 W) from room temperature to 100 °C over 3 minutes and kept at the temperature for 30 min with a maximum of 900 W heating power to obtain a Zr-node solution. The mixture was allowed to cool down to room temperature and TBAPy (80 mg) and TFA (500 µL) were added. The complete mixture was then heated from room temperature to 150 °C with 25 °C/min ramp and kept at that temperature for 60 min with maximum heating power of 900 W. After cooling down back to room temperature, solid NU-1000 was separated from the solvent by centrifugation using an Eppendorf 5810 R9 Centrifuge at 4000 rpm giving 3220 g for 30 min at 5 °C. These conditions were also used in further separation steps. The solid was washed using two cycles of washing (DMF, 30 mL) and centrifugation. The washed NU-1000 was mixed with DMF (40 mL) and concentrated HCl (2 mL) to remove the benzoate modulators. The mixture was sonicated for 15 min and soaked for another hour and finally separated by centrifugation. The obtained NU-1000 was then washed three times with 30 mL of acetone to exchange solvent before it was dried in air at 80 °C overnight to obtain the final product (see yields in Table S2).

1.4 NU-1000-TFA synthesis

An earlier report of NU-1000-TFA synthesis was followed with minor changes[1]. NU-1000 (50 mg) was suspended in DMF (3 mL) and TFA (620 µL) was added. The mixture was incubated and stirred at 60 °C on a hotplate for 18 h. After cooling down to room temperature, the mixture was centrifuged and washed 3 times with DMF, followed by one acetone wash and soaking in 30 mL of acetone overnight. The NU-1000-TFA product was centrifuged and dried in air at 80 °C overnight.

1.5 Characterisation of NU-1000

1.5.1 Linker to Zr ratio

The linker:Zr ratio for NU-1000 was calculated following a reported method[2] using equation 1, where n_L is the number of linkers per node, mol_L is the total amount of linkers, mol_{Zr} is the total amount of Zr and the 6 factor accounts for the number of Zr atoms in each metal node.

$$n_L = 6 \cdot \frac{mol_L}{mol_{Zr}} \quad (1)$$

Data from TGA analysis (Figure S4) was used to calculate the linker:Zr ratio comparing weight percent (wt%) of dehydrated NU-1000 (DH NU-1000) slightly before decomposition at 430 °C and after full

decomposition at 800 °C (dash lines Figure S4) where only ZrO_2 is expected to remain[2]. Using equation (1) we obtained a linker:Zr ratio equal to 1.88:1 (for NU-1000) and 1.98:1 (for NU-1000-TFA), which are in agreement with theoretical ratio of 2:1[3].

$$n_L = 6 \text{ x } \left[\left(w\%_{DH\ NU-1000} - w\%_{ZrO_2}\right)/M_w^L\right]/\left(\ w\%_{ZrO_2}/M_w^{ZrO_2}\right)$$

$$n_L = 6 \text{ x } [(79.43 - 29.03)/682.67]/(\ 29.03/123.22) = 1.88$$

1.5.2 TFA to metal node ratio via thermogravimetric analysis

The TFA:Zr ratio for NU-1000-TFA was calculated following a method above using equation 2, where n_{TFA} is the number of TFA molecules per node, mol_{TFA} is the total amount of TFA, mol_{Zr} is the total amount of Zr and the 6 factor accounts for the number of Zr atoms in each metal node.

$$n_{TFA} = 6 \cdot \frac{mol_{TFA}}{mol_{Zr}} \tag{2}$$

Data from TGA analysis (Figure S4B) was used to calculate the TFA:Zr ratio comparing weight percent (wt%) corresponding to the loss of TFA between 300 °C (DH NU-1000-TFA, purple dash line) and 400 °C (DH NU-1000, red dash line) and after full decomposition at 800 °C (blue dash line) where only ZrO_2 is expected to remain. Using equation (2) we obtained a TFA:Zr ratio equal to 3.41 which are in agreement with theoretical ratio of 4:1.

$$n_L = 6 \text{ x } \left[\left(w\%_{DH\ NU-1000-TFA} - w\%_{DH\ NU-1000} - w\%_{ZrO_2}\right)/M_w^{TFA}\right]/\left(\ w\%_{ZrO_2}/M_w^{ZrO_2}\right)$$

$$n_L = 6 \text{ x } [(93.41 - 79.11)/114]/(\ 27.18/123.22) = 3.41$$

1.5.3 TFA to metal node ratio via ^{19}F NMR spectroscopy

Analysis of ^{19}F NMR spectroscopy (Figure S6) is summarised below:

^{19}F NMR (376.44 MHz, d_8-DMSO):

TFA: δ: -75.2 ppm, 3F, experimental integration: 0.758

TFT: δ: -61.0 ppm, 3F, experimental integration: 1.000

Given the amount of TFT standard used (0.16 µL, 1.30 µmol), the amount of TFA in the sample was:

$$n(TFA) = \frac{1.00}{0.758} \cdot 1.30\ \mu mol$$

$$n(TFA) = 1.72\ \mu mol$$

The number of TFA molecules per metal node can be determined by simple theoretical calculations. The total mass of NU-1000 increases upon TFA treatment with one molecule of water released per each molecule of TFA added (i.e., $Zr_6(\mu_3\text{-}OH)_4(\mu_3\text{-}O)_4(H_2O)_4(OH)_4(TBAPy)_2$ + TFA → $Zr_6(\mu_3\text{-}OH)_4(\mu_3\text{-}O)_4(H_2O)_{(4-n)}(TFA)_n(OH)_4(TBAPy)_2$ – $n2H_2O$). Therefore, depending on the number of TFA molecules per node (*n*) one can expect the total mass of NU-1000 to increase according to equation (2).Table S1 shows the expected values obtained for each theoretical *n* value.

$$M_{NU-1000-TFA} = M_{NU-1000} + n(M_{TFA} - M_{2H_2O}) \quad (2)$$

Table S1. Theoretical calculations to obtain the TFA to metal node ratio (*n*).

Entry	Mass of NU-1000-TFA (g mol^{-1})	*n*	Expected TFA mass (g mol^{-1})	Mass ratio NU-1000-TFA/TFA
i	2254.8	1	114.0	19.8
ii	2332.8	2	228.0	10.2
iii	2410.8	3	342.0	7.0
iv	2488.8	4	456.0	5.5

Using the amount of TFA determined experimentally (1.74 μmol) and the total mass of NU-1000-TFA used, we obtained a NU-1000-TFA to TFA ratio equal to 5.5, which corresponds to 4 TFA molecules per node in the sample (entry iv, Table S1).

1.6 Catalyst preparation using electrophoretic deposition

The preparation of catalyst films via electrophoretic deposition was carried out as follows: A suspension of MOF (50 mg) in acetone (50 mL, 1 mg mL^{-1}) was sonicated for 15 minutes. Then, a granule of I_2 (~10 mg) was added to the suspension and further sonication was performed for an additional 2 minutes. Subsequently, two FTO glass slides (length: 1.5 cm, width: 2 cm) were attached to PTFE plated Pt electrode holders arranges facing each other and placed 2 cm apart, ensuring their conductive surfaces were exposed. Approximately two-thirds of the plates were submerged into the suspension, aiming for a coverage of 2 cm^2 surface area of NU-1000 thin film on the cathode slide surface. The anode and cathode were connected to a Digimess SM5020 power supply, and a voltage of 10 V was applied for 5 minutes to deposit an even film of NU-1000 on the surface of the slide. For NU-1000-TFA, comparable thin film and loading were obtained using a voltage of 20 V and a deposition time of 2 minutes. During the application of voltage, the interaction of I_2 with acetone resulted in the release of I^- and H^+, causing the charging of NU-1000 and subsequent deposition on the cathode.[4] After the deposition process, the slides were dried in an oven at 80 °C overnight to evaporate the acetone. The loading of NU-1000 on the FTO slide was determined to be approximately 280 ± 10 μg, while for NU-1000-TFA was 300 ± 10 μg, giving 145 and 150 μg cm^{-2} loading, respectively.

1.7 Photocatalytic CO_2 reduction

The photocatalytic activities of the MOFs were evaluated in a custom-made flow reactor (Figure S7) with inline detection of products. Typical experiments were performed in a 28.5 mL round-bottom glass cylinder reactor (H:4.5 cm, D: 3.0 cm) where FTO glass slides (with a MOF thin film) were placed inside the reactor in a vertical position and irradiated at 90 degrees with a 365 nm LED providing 1.8 W cm^{-2} of irradiance. The reactor was purged with Ar until residual air is removed (around 2 hours). Ultrapure CO_2 (99.9995%) was bubbled through a milli-Q water bubbler before entering the reactor. Typically, samples were firstly irradiated under Ar (2 sccm) for 2 hours, and then exposed to wet CO_2 and Ar flow mixtures (1:1 mass flow ratio maintaining the total flow rate). Concentration of the effluent gas as a function of irradiation time by inline gas chromatography starting an injection program 1 min prior to turning on the light and then with 10 minute intervals from the moment when the light was turned on. Control reactions (without CO_2, light or water) were carried out adjusting Ar flow rate to 2 sccm. Relative humidity (RH) was measured under control and reaction conditions, giving values of 20 % and 30 %, respectively. Under reaction conditions, molar proportions of Ar, CO_2, and water were 57.2, 42.1 and 0.7 %, respectively, comparing a CO_2 peak area under 100 % CO_2 environment to calibration curve, assuming water concentration to be same as in 30 % RH under air at 20 °C and 1 bar conditions. Water concentration in reaction conditions was estimated according to psychromatic chart under ambient pressure[5].

1.8 GC Calibration and product quantification

A gas mixture containing CO_2, CO, N_2, H_2, CH_4, CH_3CH_3, and $CH_3CH_2CH_3$ was injected into the chromatographer at different known concentrations and a calibration curve was created. During the reaction conditions, the peak area of CH_4 was compared to the calibration curve to obtain CH_4 formation rate in each data point. This is, from the calibration curve we determined the number of moles of CH_4 (n_{CH4}) and considering the flow rate used (Q = 2 sccm) and the total volume of the reactor (V_R = 36.5 mL) we can determine the rate of CH_4 formation (r_{CH4}) using equation (3). These values are plotted in Figure S10.

$$r_{CH_4} = \frac{n_{CH_4}}{V_R}\, Q \tag{3}$$

The amount of CH_4 per gram of catalyst was calculated by dividing the number of CH_4 mol produced by the average MOF amount (ca 300 μg). To avoid overestimations of the CH_4 production rate, the amount of CH_4 produced in dry conditions was subtracted from the total amount measured under wet CO_2 conditions. For this, we averaged the CH_4 rate found between 60 and 120 min (136 μmol g^{-1} h^{-1}).

1.9 Isotope-tracer experiments

$^{13}CO_2$ (^{13}C 99%) was purchased from Cambridge Isotope Laboratories, Inc. In a purged reactor, a NU-1000 thin film was first irradiated under Ar (1 sccm) for 2 hours. The irradiation was then paused, and the sample was exposed to wet $^{13}CO_2$ and Ar flow mixtures (1:1 mass flow ratio maintaining the total flow rate). Subsequently, the reactor was sealed and subjected to irradiation for an additional 17 hours to allow for accumulation of products. After irradiation, the evolved gases were analysed via online mass spectrometry. The following m/z values were used to detect each product: m/z = 16 for CH_4, m/z = 17 for $^{13}CH_4$, m/z = 18 for H_2O, m/z = 29 for ^{13}CO, m/z = 44 for CO_2 and m/z = 45 for $^{13}CO_2$. A control experiment was performed in absence of both catalyst and light. The reactor and irradiation source used are the same as those employed in the photocatalytic CO_2 reduction experiments (see section 1.7).

Figure S11 shows the MS analysis of the gases obtained after the photocatalytic transformation of wet $^{13}CO_2$ by NU-1000 (Figure S11A) and a blank experiment in the absence of catalyst and light (Figure S11B). We observe that the main difference between the photocatalyzed reaction and the blank MS spectra lies in the increase in the m/z = 17 peak, attributed either to $^{13}CH_4$ or ^{16}OH (fragment of H_2O). Ratios of m/z 17 to 18 were calculated to discount the contribution of the signal corresponding to ^{16}OH, obtaining a value 46 % bigger for the photocatalyzed reaction, indicating formation of $^{13}CH_4$. In addition, the more abundant m/z signals are 45, 29 and 16 corresponding to $^{13}CO_2$ and its fragments ^{13}CO and ^{16}O, respectively. To rule out the presence of m/z = 16 originating from $^{12}CH_4$ due to catalyst degradation, we calculated the ratio between m/z signals 16 and 45. This ratio remains almost constant, being 0.17 and 0.21 for the catalytic experiment and the blank, respectively. Therefore, we do not detect formation of $^{12}CH_4$ under these conditions. These results demonstrate that the methane formed during the catalytic processes is due to CO_2 reduction and not related to catalyst decomposition.

2 Supporting Figures

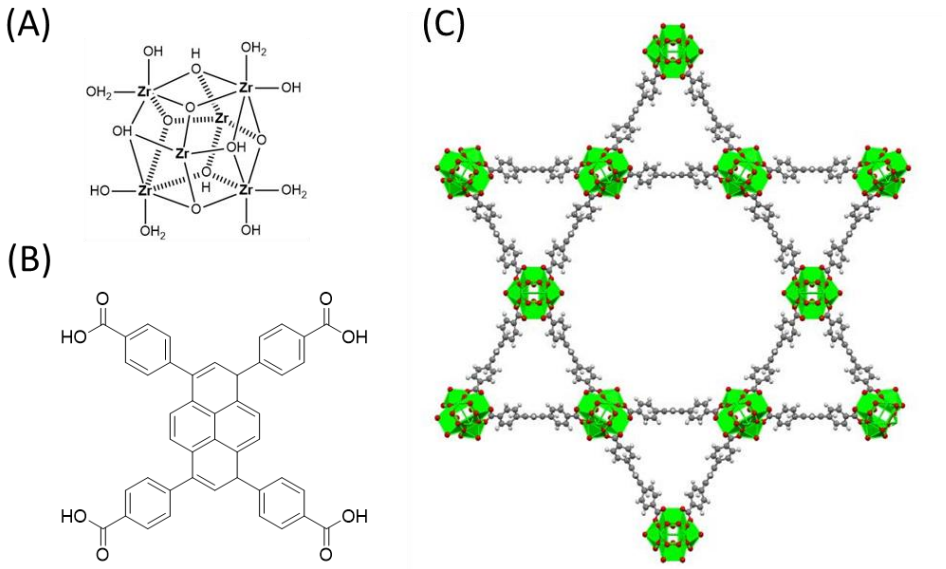

Figure S1. (A) Fully hydrated $Zr_6O_4(OH)_4$ node, (B) Tetrakis-(*p*-benzoic acid)pyrene (TBAPy) linker, (C) NU-1000 mesoporous structure (Zr_6O_8 nodes shown in green).

Table S2. Screening of experimental conditions for the synthesis of NU-1000.[a]

Entry	Volume (mL)	TFA:M ratio	Time (h)	Yield (%)
1[b]	8	1.7	18	38.3
2	8	2.6	0.5	28.7
3	20	16.8	0.75	57.5
4	20	21	0.75	53.6
5	**20**	**21**	**1**	**78.8**
6	20	21	1	76.2

[a]Reaction conditions: Preparation of Zr-node: 200 mg $ZrOCl_2$, 3.0 g of benzoic acid (BA), 40 mL of DMF, heated to 100 °C at 25 °C min^{-1} and kept at 100 °C for 30 min. Preparation of MOF: Zr-node solution, 80 mg of TBAPy (ligand), corresponding volume of TFA, heated to 150 °C at 25 °C min^{-1} and kept for at 150 °C for the corresponding amount of time. [b] Synthesis performed following a conventional heating method previously reported (BA:M = 54.6).[6]

Table S3. Optimisation of MWA method for scaled-out synthesis of NU-1000.

Original Entry	Volume (mL)	BA:M ratio	TFA:M ratio	Yield (%)
1	10	40	4.2	40
2	10	40	8.4	47
3	10	40	16.8	78
4	10	13	8.4	-
5	10	27	8.4	-
6	10	53	8.4	76
7	40	40	10.5	87
8	40	40	10.5	79
9	40	40	10.5	82
10	40	40	10.5	85
11	40	40	10.5	73
12	40	40	10.5	96
13	40	40	10.5	93
14	40	40	10.5	97
15	40	40	10.5	96
16	40	40	10.5	92

Reaction conditions: Preparation of Zr-node: 200 mg $ZrOCl_2$, corresponding mass of benzoic acid (BA), 40 mL of DMF, heated to 100 °C at 25 °C min^{-1} and kept at 100 °C for 30 min. Preparation of MOF: Zr-node solution, 80 mg of TBAPy (ligand), corresponding volume of TFA, heated to 150 °C at 25 °C min^{-1} and kept at 150 °C for 60 min. Ethanol (E) or acetone (A) were used to wash NU-1000 after modulator removal. All further syntheses of NU-1000 were done following conditions of entry 7.

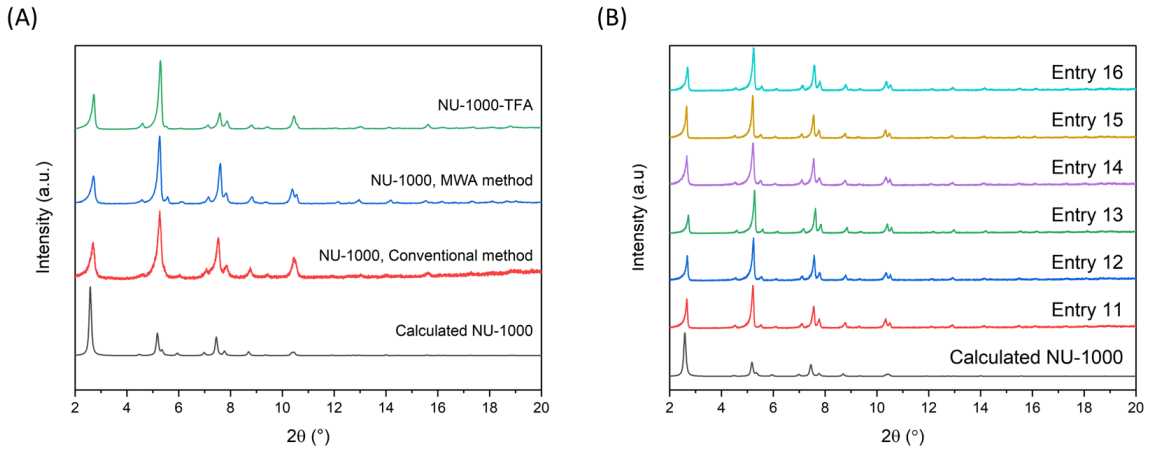

Figure S2. PXRD patterns of (A) Conventional, MWA synthesised NU-1000 and NU-1000-TFA (prepared by post-synthetical functionalization of MWA synthesised NU-1000 (B) scaling-out MWA synthesis. Synthesis conditions for entries shown in (B) are in Table S3.

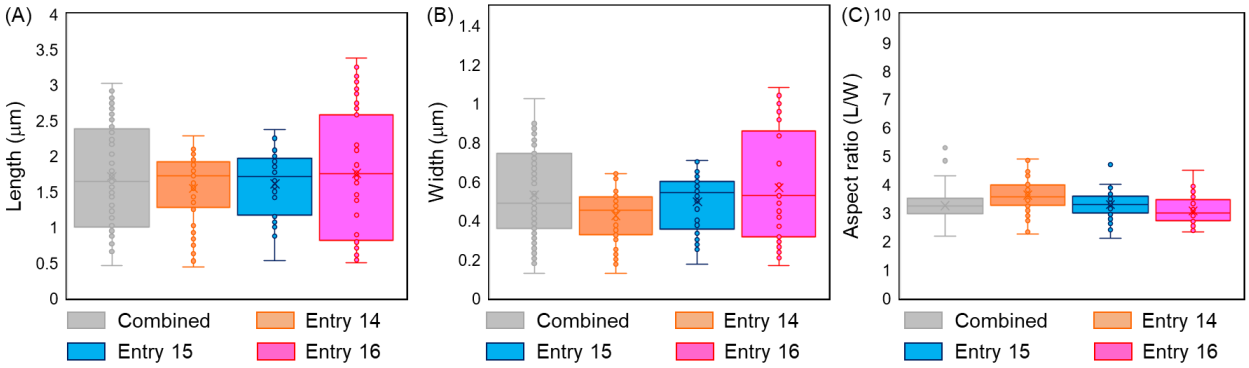

Figure S3. Box and whisker plots of particle sizes from SEM images of different MWA synthesised NU-1000 to define (A-C) length, width, and aspect ratio for entries 14-16 shown in Table S3. The distribution was defined by choosing fifty particles in an arbitrary manner from at least 5 SEM images from different parts of the sample. Error bars represent the largest and smallest particle sizes. Boxes represent the interquartile range (outer line) and median (central line) particle sizes. Mean is denoted by an x. Datapoints beyond the highest and lowest limits are outliers.

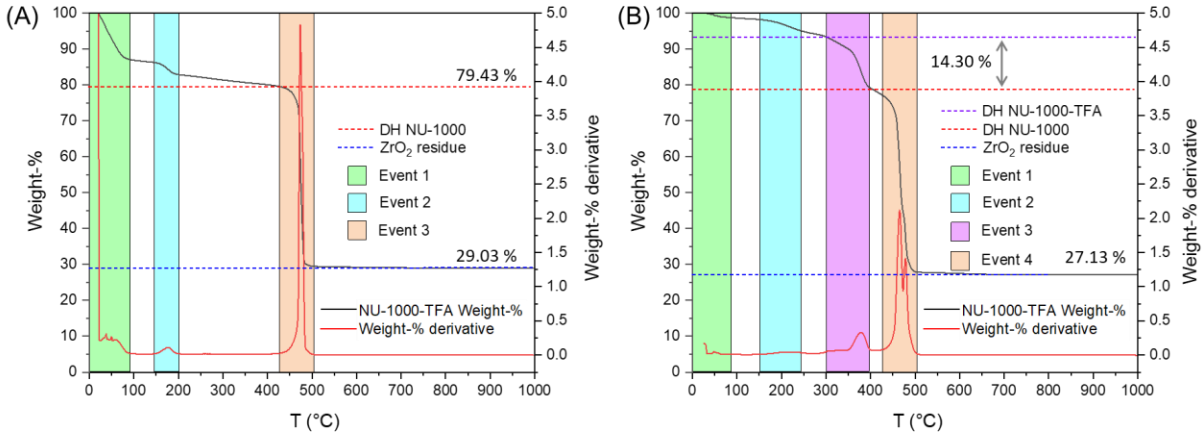

Figure S4. Thermogravimetric analysis (TGA) under air with remaining weight-% of a dehydrated (DH) sample before (red) and after (blue) thermal de-composition for (A) NU-1000 and (B) NU-1000-TFA. Dash lines indicate values used for calculations of the linker:Zr ratio and the TFA:Zr ratio.

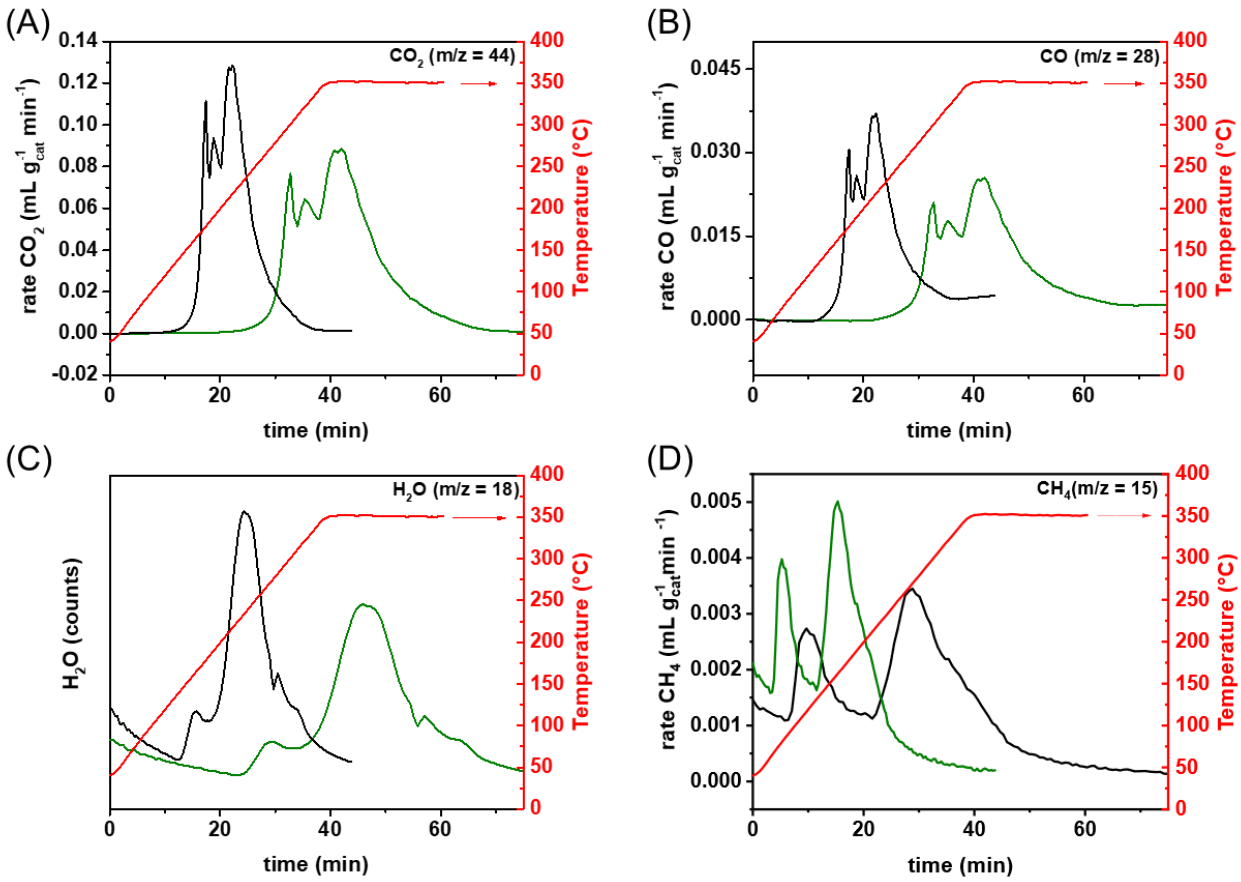

Figure S5**.** Temperature programmed desorption (TPD) profile mass spectrometry signal of (A) CO_2, (B) CO, (C) H_2O and (D) CH_4 on NU-1000 (black) and on NU-1000-TFA (green) against time and temperature (red). Water was not quantified due to instrumental limitations to inject water vapour with known flow rate.

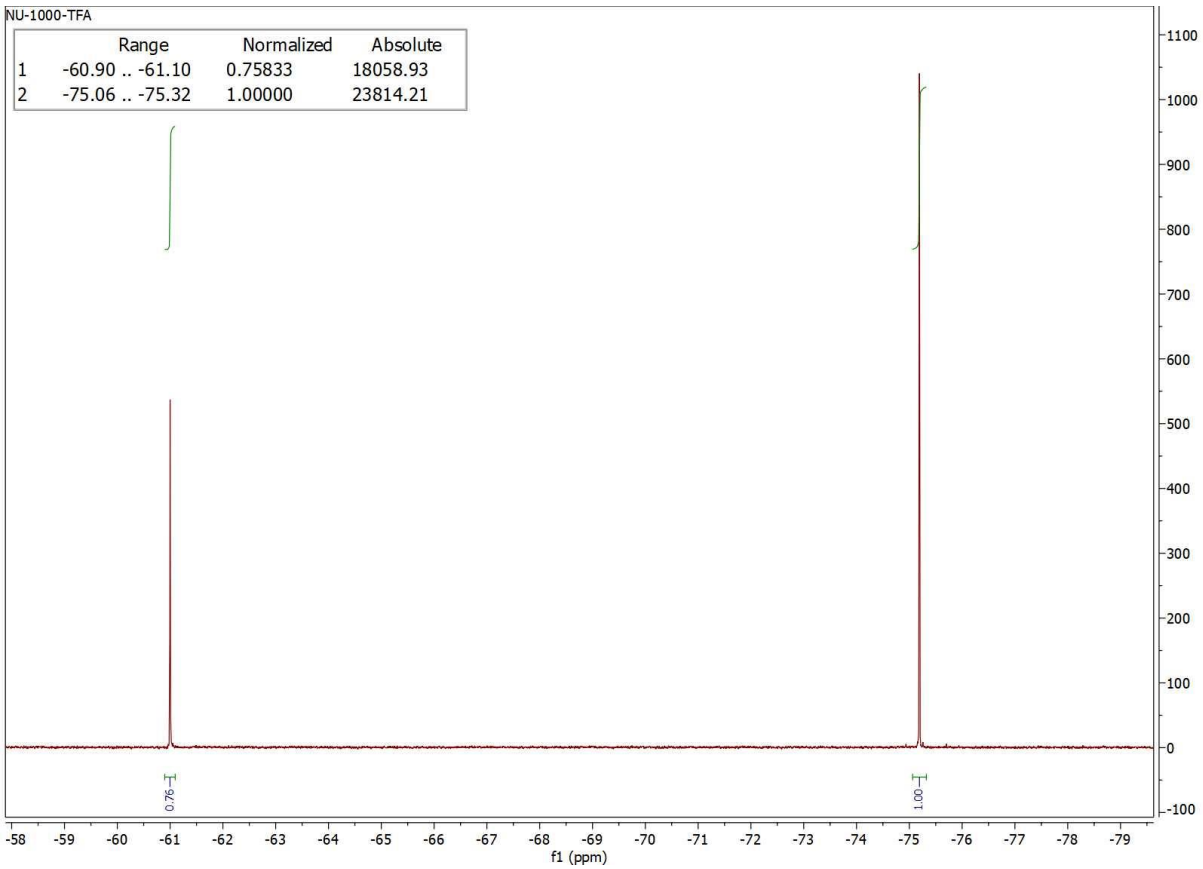

Figure S6. ^{19}F NMR spectrum of NU-1000-TFA in deuterated DMSO. Sample preparation: 1.11 mg NU-1000-TFA digested in 6 droplets of D_2SO_4 were mixed with 0.16 µL trifluorotoluene (TFT) as an internal reference and 0.6 mL of deuterated DMSO. ^{19}F NMR (376.44 MHz, d_8-DMSO): δ: -75.2 ppm (TFA), δ: -61.0 ppm (TFT).

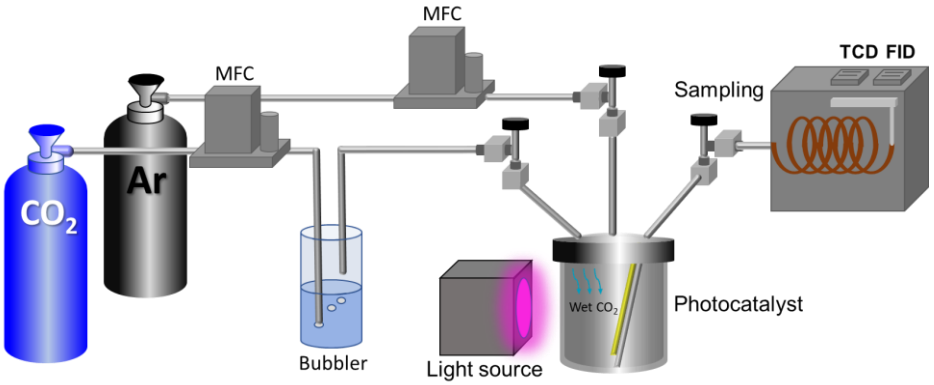

Figure S7. Reactor setup used in the photocatalytic experiments.

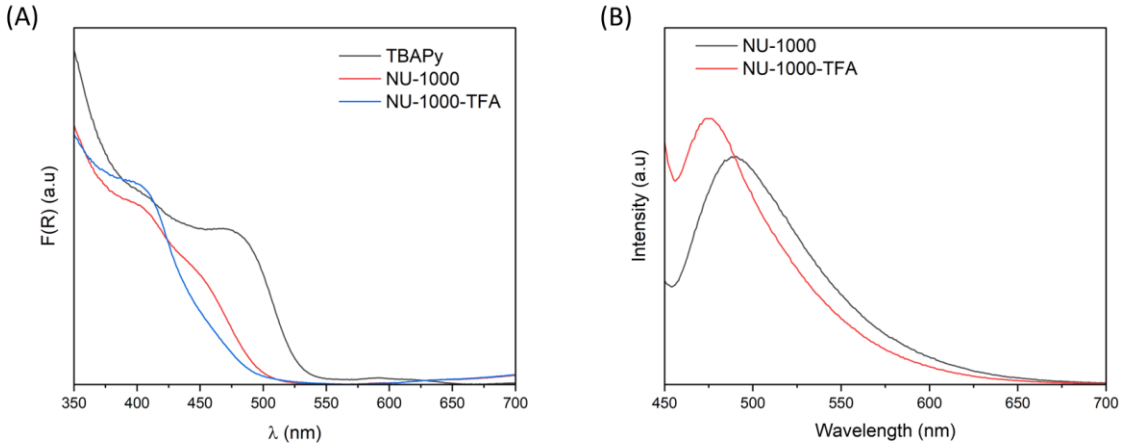

Figure S8. (A) UV-Vis diffuse reflectance spectra for linker (TBAPy), NU-1000 and NU-1000-TFA and (B) photo-luminescence spectra (λ_{exc}: 400 nm) of NU-1000 and NU-1000-TFA.

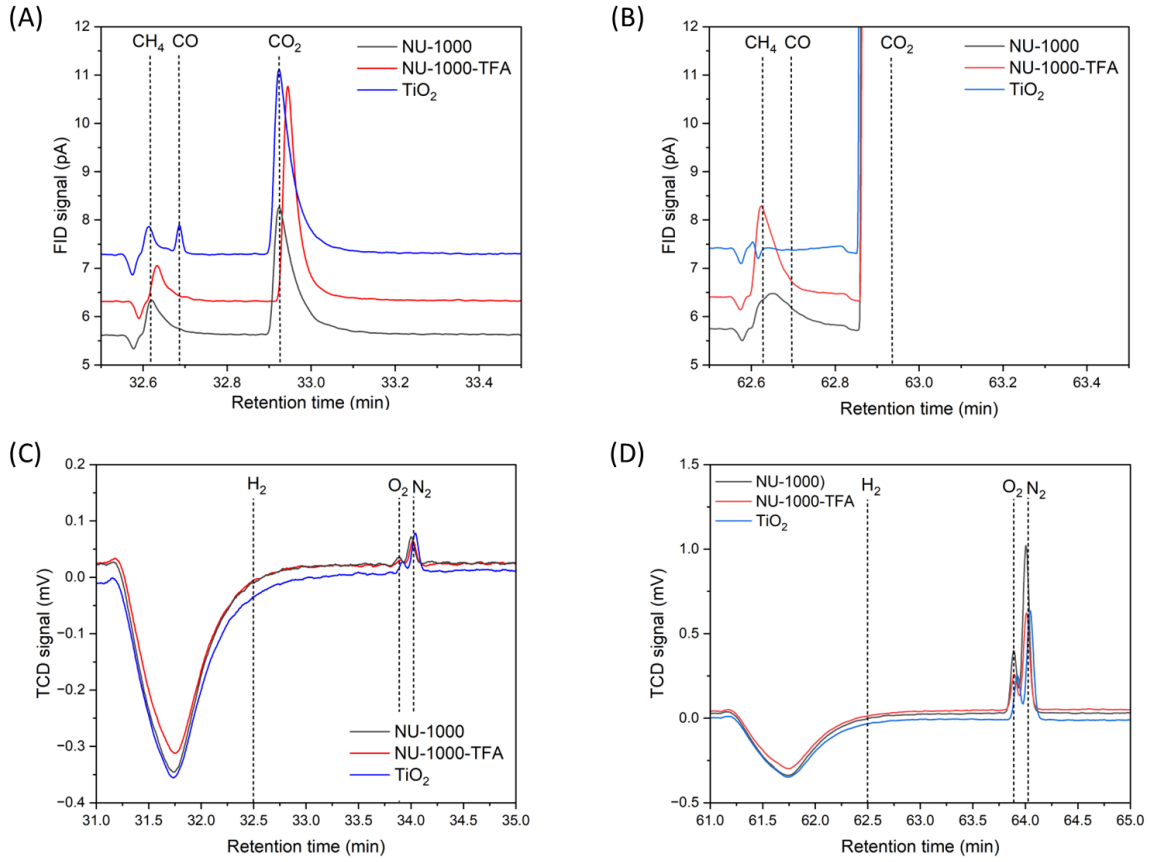

Figure S9. Chromatograms showing the in line detection of gases using flame ionisation detection (FID) after (A) 30 min of UVA (365 nm) irradiation under Ar and after (B) 60 min irradiation (365 nm) under reaction conditions shown in Table 1 (i.e., catalyst (area: ~2 cm^2, thickness: 22 μm, mass: 300 μg), Ar (1 sccm), wet CO_2 (1 sccm) (RH ~30%), 365 nm LED irradiation (1.8 Wcm^{-2}, ~1 cm^2 spot)) for NU-1000, NU-1000-TFA and TiO_2; and using thermal conductivity detection (TCD) after (C) 30 min irradiation under Ar and after (D) 60 min irradiation under reaction conditions for NU-1000, NU-1000-TFA and TiO_2. Gases detected by FID: CH_4: 1.63 min, CO: 1.7 min and CO_2: 1.9 min; and detected by TCD: H_2: 1.5 min, O_2: 2.9 min and N_2: 3.0 min. Samples were injected at 31.0 min under Ar (A and C) and at 61.0 min under reaction conditions (B and D).

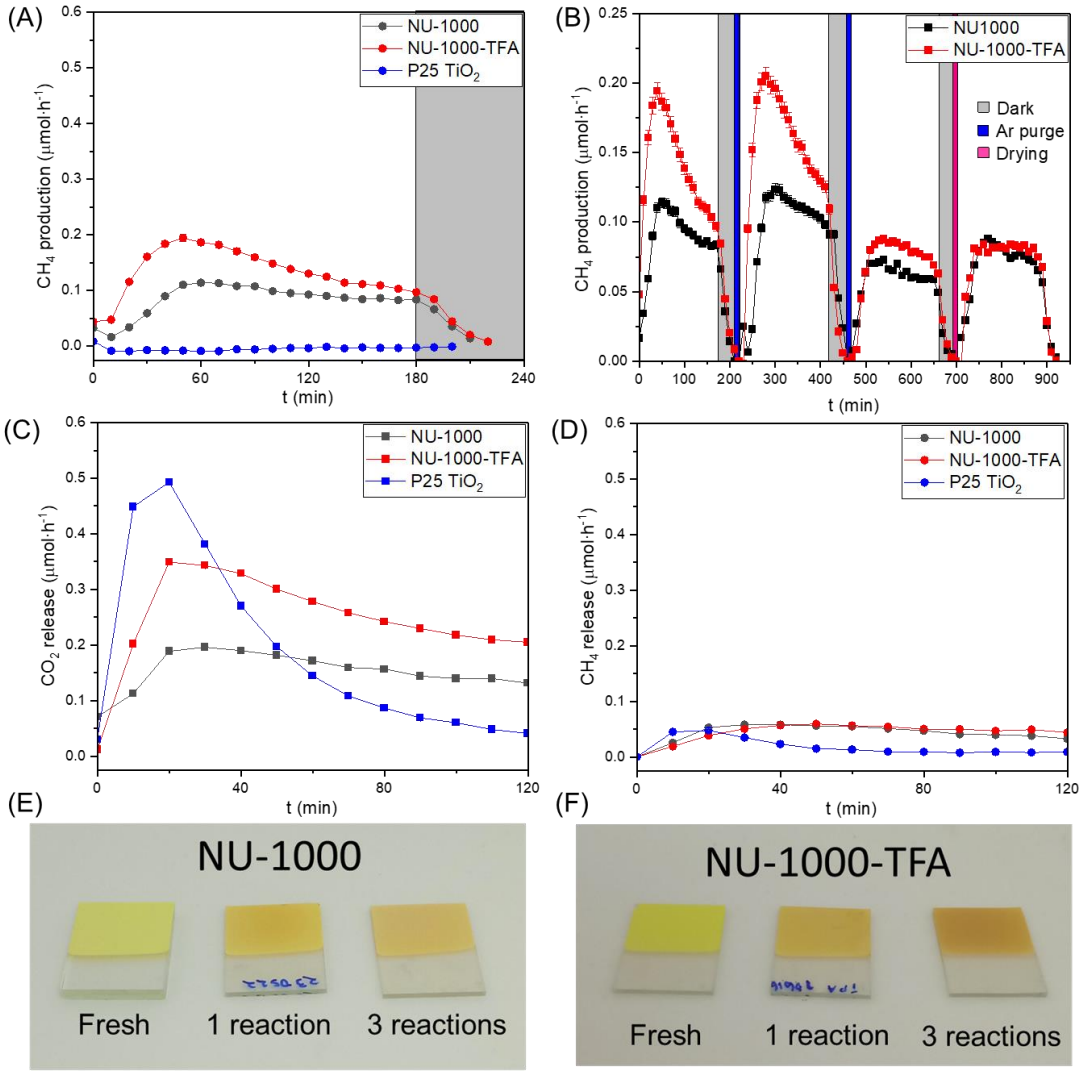

Figure S10**.** (A) CH_4 production over NU-1000, NU-1000-TFA, and TiO_2, showing that when irradiation is discontinued (grey area) the CH_4 production stops. (B) CH_4 production over NU-1000, NU-1000-TFA in recycling experiments over a total of four reaction cycles (cleaning processes as shown in D, the catalyst was dried in oven before the last cycle). (C,D) Catalyst cleaning process showing CO_2 and CH_4 release from surface of NU-1000, NU-1000-TFA, and TiO_2, (E) Picture of NU-1000 and of (F) NU-1000-TFA before the reaction and after 1 and 3 CO_2 reduction cycles. Reaction conditions: catalyst (area: ~2 cm^2, thickness: 22 μm, mass: 300 μg), Ar (1 sccm), wet CO_2 (1 sccm) (RH ~30%), 365 nm LED irradiation (1.8 Wcm^{-2}, ~1 cm^2 spot), as described in Table 1.

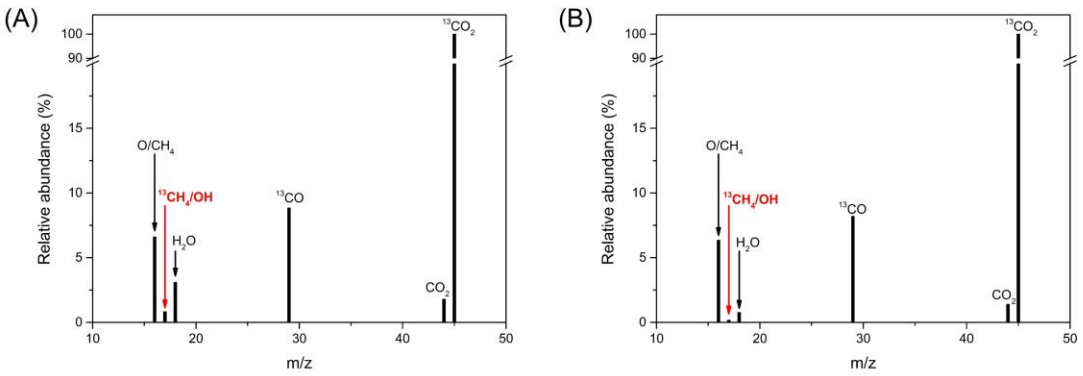

Figure S11. Mass spectra showing (A) the photocatalyzed transformation of wet $^{13}CO_2$ into $^{13}CH_4$ by NU-1000 (reaction conditions: catalyst (area: ~2 cm^2, thickness: 22 mm, mass: 300 mg), 1:1 ratio of Ar and wet $^{13}CO_2$ (RH ~30%) in a sealed reactor, 365 nm LED irradiation (1.8 Wcm^{-2}, ~1 cm^2 spot)) and (B) control experiment in absence of both catalyst and light (conditions: 1:1 ratio of Ar and wet $^{13}CO_2$ (RH ~30%) in a sealed reactor). Relative abundances for m/z 17 of 0.82 and 0.17 % were determined for (A) and (B), respectively indicating formation of $^{13}CH_4$. The more abundant m/z signals are 45, 29 and 16 corresponding to $^{13}CO_2$ and its fragments ^{13}CO and ^{16}O, respectively. As relative abundance of m/z 16 and 29 remain constant between (A) and (B), we do not detect formation of $^{12}CH_4$ or ^{13}CO under these conditions. These results demonstrate that the methane formed during the catalytic processes is due to CO_2 reduction and not related to catalyst decomposition.

Table S4. Previously reported photocatalytic reduction of CO_2 using MOF-based materials.

Material	Reaction media	Excitation (nm)	Gauge pressure (bar)	CH_4 Yield (µmol/g/h)	CO yield (µmol/g/h)	HCOOH yield (µmol/g/h)	Ref
NU-1000	**Wet CO_2**	**365**	**0**	**167**	**Traces**	-	**This work**
NU-1000-TFA		**365**		**823**	**Traces**	-	
Fe-TCPP@NU-1000	CO_2/TEOA/CH_3CN	390	N/R		1867	-	[7]
NU-1000					23.3		
PCN-222(Ni)@UiO-67-NH_2	Wet CO_2	≥420	N/R	10.8	10.3	146	[8]
PCN-222(Ni)				3.6	2.7	54.3	
UiO-67-NH_2				2.3	7.2	18	
NH_2-MIL-125(Ti)	Wet CO_2		N/R	2.23	36.22		[9]
g-C_3N_4-RGO-NH_2-MIL-125(Ti)				3.45	95.95	-	
UiO-66-PA-3	CO_2/TEOA/CH_3CN	420-800	N/R	-	-	92.6	[10]
PCN-601	CO_2/H_2O vapour	Solar simulation (AM1.5)	0.8	92.0	3.2	-	[11]

Wet CO_2: CO_2 bubbled through H_2O and then introduced to reactor. CO_2/H_2O vapour: Liquid water at the bottom of the reactor. N/R: not reported.

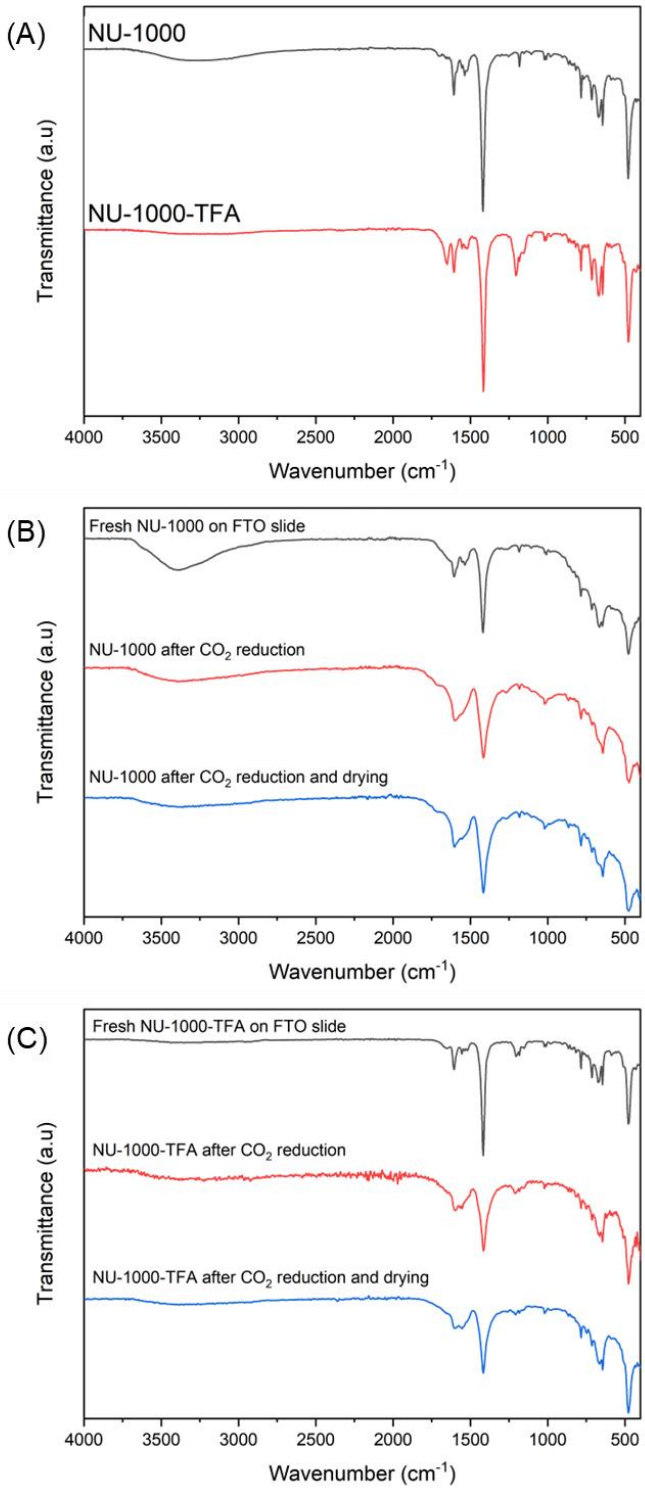

Figure S12**.** FT-IR of (A) fresh powder samples of NU-1000 and NU-1000-TFA, (B) NU-1000 thin film samples on FTO slide before, after 1 reaction cycle and after drying the used catalyst at 80 °C overnight (C) NU-1000-TFA thin film samples on FTO slide before, after 1 reaction cycle and after drying the used catalyst at 80 °C overnight.

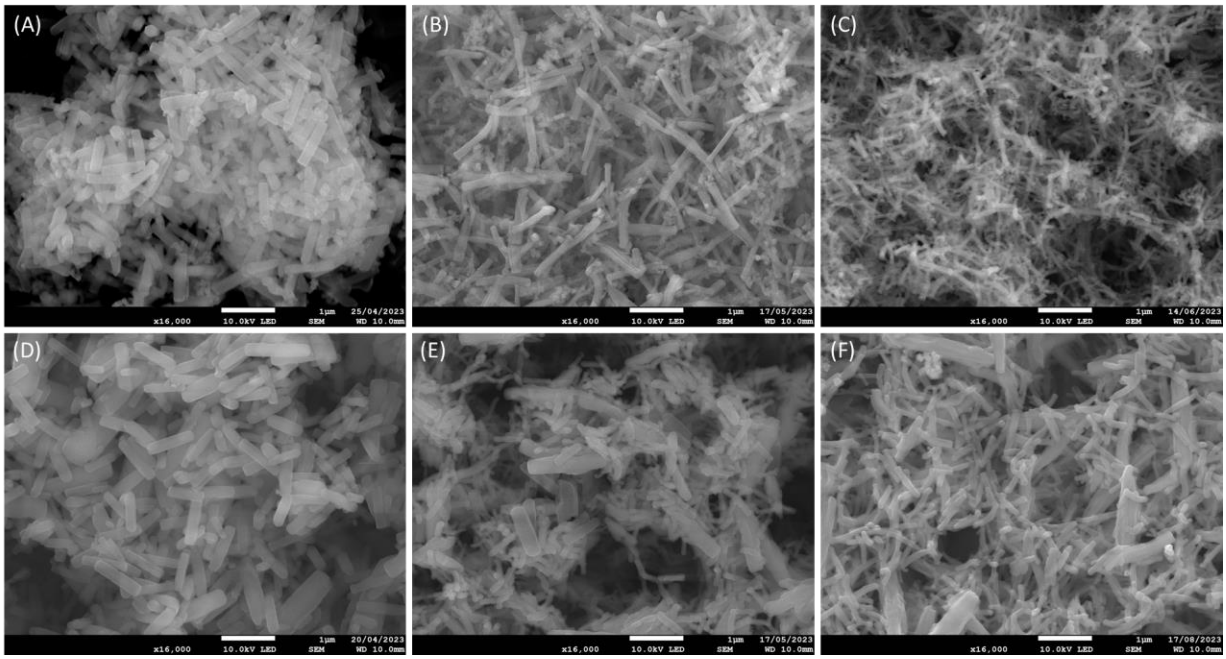

Figure S13. SEM images of (A) fresh NU-1000 and used NU-1000 catalyst after (B) 1 reaction and (C) 4 reaction cycles, (D) fresh NU-1000-TFA and used NU-1000-TFA after (E) 1 reaction cycle and (F) 4 reaction cycles.

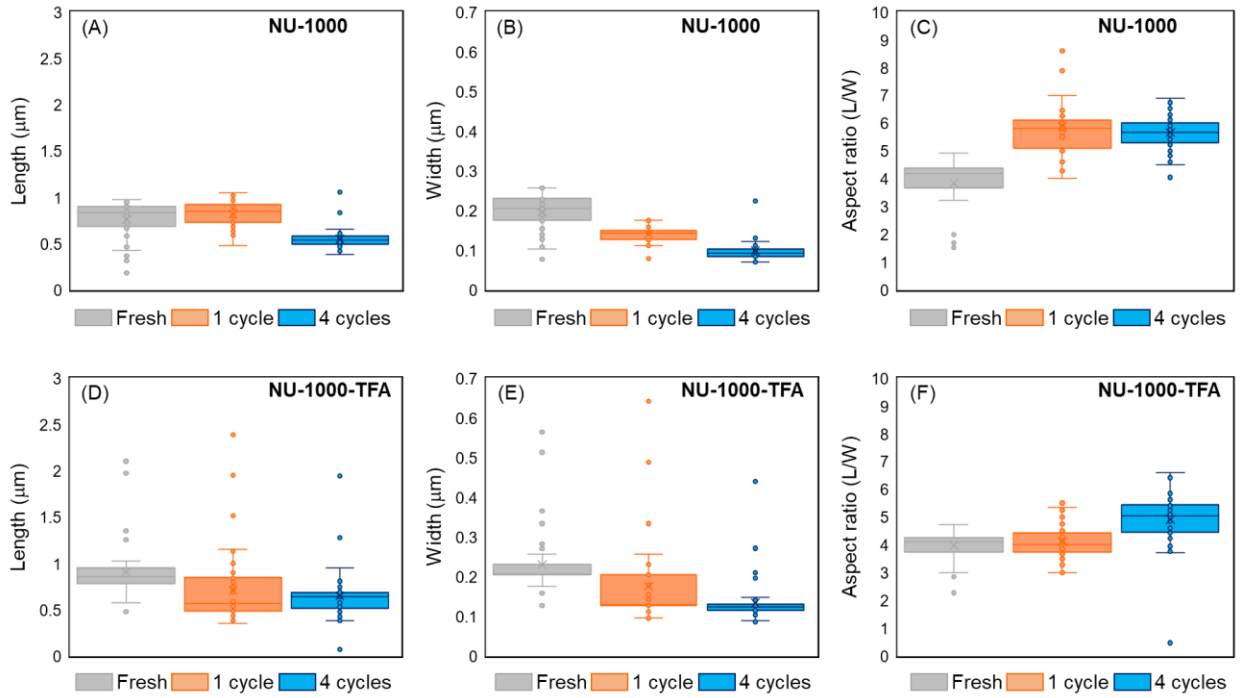

Figure S14. Box and whisker plots of particle sizes from SEM images for length, width, and aspect ratio distributions of (A-C) NU-1000 and (D-F) NU-1000-TFA on FTO slides before (fresh) and after one or four CO_2 reduction cycles. The distribution was defined by choosing particles in an arbitrary manner from at least 5 SEM images from different parts of the sample. Boxes represent the interquartile range (outer line) and median (central line) particle sizes. Mean is denoted by an x. Datapoints beyond the highest and lowest limits are outliers.

3 References

[1] L. Yang, K. B. Idrees, Z. Chen, J. Knapp, Y. Chen, X. Wang, R. Cao, X. Zhang, H. Xing, T. Islamoglu, O. K. Farha, *ACS App. Nano Mater.* **2021**, *4*, 4346-4350.

[2] I. A. Lázaro, *Eur. J. Inorg. Chem.* **2020**, *2020*, 4284-4294.

[3] J. E. Mondloch, W. Bury, D. Fairen-Jimenez, S. Kwon, E. J. DeMarco, M. H. Weston, A. A. Sarjeant, S. T. Nguyen, P. C. Stair, R. Q. Snurr, O. K. Farha, J. T. Hupp, *J. Am. Chem. Soc.* **2013**, *135*, 10294-10297.

[4] L. Grinis, S. Dor, A. Ofir, A. Zaban, *J. Photochem. Photobiol. A* **2008**, *198*, 52-59.

[5] M. Bomberg, T. Kisilewicz, C. Mattock, *Metods of Building Physics*, Cracow University Press, **2015**.

[6] T. Islamoglu, K. Otake, P. Li, C. T. Buru, A. W. Peters, I. Akpinar, S. J. Garibay, O. K. Farha, *CrystEngComm* **2018**, *20*, 5913-5918.

[7] K. Zhang, S. Goswami, H. Noh, Z. Lu, T. Sheridan, J. Duan, W. Dong, J. T. Hupp, *J. Photochem. Photobiol.* **2022**, *10*, 100111.

[8] H. B. Huang, Z. B. Fang, R. Wang, L. Li, M. Khanpour, T. F. Liu, R. Cao, *Small* **2022**, *18*, e2200407.

[9] R. R. Ikreedeegh, M. Tahir, *J. Environ. Chem. Eng.* **2021**, *9*, 105600.

[10] Y. Du, G. a. Jie, H. Jia, J. Liu, J. Wu, Y. Fu, F. Zhang, W. Zhu, M. Fan, *J. Environ. Sci.* **2023**, *132*, 22-30.

[11] Z. B. Fang, T. T. Liu, J. Liu, S. Jin, X. P. Wu, X. Q. Gong, K. Wang, Q. Yin, T. F. Liu, R. Cao, H. C. Zhou, *J. Am. Chem. Soc.* **2020**, *142*, 12515-12523.